This Project has received funding from European Commission by means of Horizon 2020,
the EU Framework Programme for Research and Innovation, under Grant Agreement no.727348

Grant Agreement No. 727348

Project Acronym:

SOCRATCES

Project title:

SOlar Calcium-looping integRAtion for Thermo-Chemical Energy Storage.

DELIVERABLE D3.3

CSP-Calciner integration model

Funding scheme:	Research and Innovation Action (RIA)		
Project Coordinator:	USE		
Start date of the project:	01.01.2018	**Duration of the project:**	36 months
Contractual delivery date:	Month 12		
Actual delivery date:	28.12.2018		
Contributing WP:	WP3		
Dissemination level:	*Public*		
Authors:	Virtualmech (VM)		
Contributors:	CLX, USE, ZAR, TOR, AUTH, CERTH		
Version:	v0		
Document name	**SOCRATCES_D3.3_final**		

The sole responsibility for the content of this report lies with the authors. It does not necessarily reflect the opinion of INEA.
Neither INEA nor the European Commission are responsible for any use that may be made of the information contained therein.

Table of contents:

SCOPE

This document aims to describe the development process for a pre-design of the solar receiver, taking into account the necessary conditions (geometry, materials, etc.) to carry out properly the solar calcination, and the results obtained so far.

The deliverable summarizes the work under execution in *Task 3.4 "CSP-calciner integration"*. This task is divided into the following activities or subtasks:

- ST 3.4.1: Solar receiver geometry and location
- ST 3.4.2: Solar receiver material properties
- ST 3.4.3: Heliostat characterization
- ST 3.4.4: Solar flux simulation
- ST 3.4.5: Solar power to calciner simulation
- ST 3.4.6: Design of thermal connection between solar receiver and calciner
- ST 3.4.7: Write up of the deliverable.

The document analyses each of the subtasks and it will be used as reference for the WP6 (Engineering and construction).

It is important to note that subtask ST3.4.6 has been eliminated, since the original idea was to heat an external receiver with the solar flux and then to transfer that heat inside the reactor. Now the design considered introduces the solar flux directly into the reactor, making unnecessary this thermal connection.

The document here presented has been developed within the SOCRATCES project under the confidentiality rules of the project and consortium.

1. INTRODUCTION

The key element of the Socratces project, and what makes it a novelty, is the use of Concentrated Solar Power (CSP) to store energy in a thermochemical process.

To demonstrate the feasibility of such storage, a pilot plant will be built and operated in Seville (Spain). The demonstration plant will occupy a space plot within a research facility of the University of Seville (USE) located in the city, at the coordinates 37º22’03.61’’N-5º58’32.43’’W (see Figure 1.1).

Figure 1.1. SOCRATCES plot, space owned by USE.

The integration of CSP into the process involves two different equipment: the solar concentrator and the solar reactor.

The solar concentrator is composed of heliostats and secondary parabolic concentrator, which are well known in the solar industry and have a low degree of uncertainty.

As for the Solar Calciner Reactor, two options are currently considered, namely:

1. Indirect Calix Flash Calciner (CFC) Solar Calciner (ICFC-SC)
2. Indirect Cavity Silicon Carbide (SiC) Solar Calciner (ICSiC-SC)

Option 1 has been selected by project partners among a wide range of possible solutions, including direct CFC schemes, central tower-like cavity with pre-heated CO_2, etc. For more information on the possibilities and the final selection process, see document: *Solar-Calciner Connection Design-working document v1.1*.

After some time, Option 1 was supplemented with Option 2 with the aim to guarantee that a suitable solution can always be reached. Therefore, if Option 1 is not viable for any reason, Option 2 can be used. Besides, Option 2 has valuable scientific content that is relevant for some partners such as USE and VM, then it is meaningful for them to provide resources and study such a case, always treating it as a backup in case Option 1 is not feasible eventually.

There is an inherent uncertainty in this component, as it is a novel design and one of a kind system that has never been simulated or manufactured before, to the knowledge of the project consortium. Therefore, it seemed a good idea to have two different choices in parallel: the main one (ICFC-SC) and the backup (ICSiC-SC). Besides, at the time the selection of Option

1 was made, Option 2 was not present, as it was proposed by Carlos Tejada (Atria-VM) and USE late summer 2018, several months after Option 1 was selected.

Both options work under a beam down solar scheme where the incident rays from the heliostat field are redirected by a secondary reflector (or re-concentrator) to a vertical cavity situated just below. This vertical cavity eventually materializes into Option 1 or Option 2. In the following sections, both approaches are described in detail.

1.1. Indirect CFC Solar Calciner (ICFC-SC)

In this beam-down configuration, radiation enters the vessel from the top:

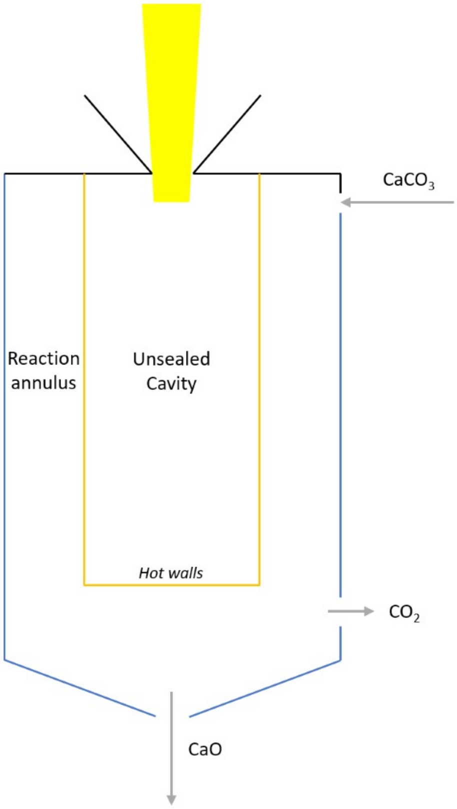

Figure 1.2. Indirect CFC Solar Calciner (ICFC-SC) scheme.

The solar flux reaches the walls of a cavity and partly is absorbed and reflected. The inner side of the wall then heats up and transfers the heat by conduction to the outer side of the wall, which in turn is the inner side of the reactor.

Reaction occurs in the cylindrical annulus between the outer shell and the inner solar cavity. An inlet stream of CO2 and limestone is injected tangentially into the cylinder, generating a vortex flow that creates a helix trajectory for the particles.

This has two advantages: increases the residence time and homogenises the heat applied to the particles, thus having a compact reactor.

The cyclone configuration of this reactor at the bottom allows removal of solid particles at the centre of the funnel, while the gas stream is extracted through the external shell.

The falling time of the particle depends on its size and density, and the inlet stream has to be studied carefully in order to achieve the desired residence time for the reaction to complete.

1.2. Indirect Cavity SiC Solar Calciner (ICSiC-SC)

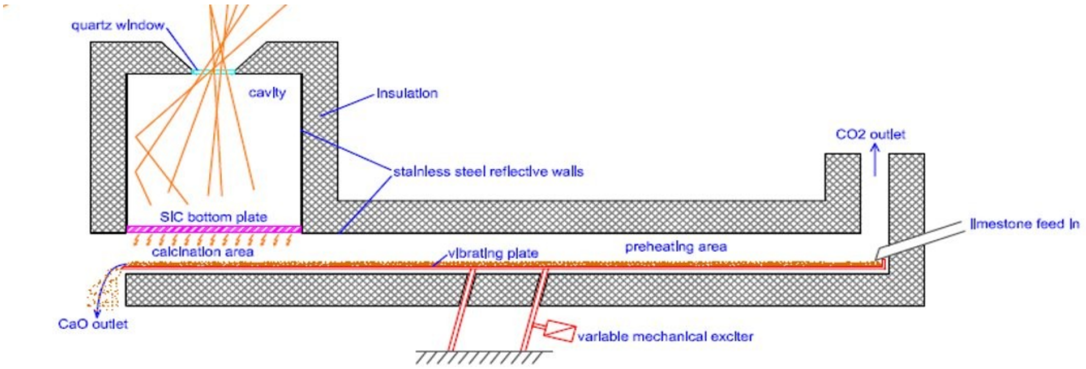

Figure 1.3. Indirect Cavity Solar Calciner (IC-SC) scheme.

In this receiver scheme, a “continuous solar furnace” concept is used, similar to other industrial processes that require working in a continuous basis, and easily scalable for a larger calciner.

The receiver can be divided in three sections: the receiver cavity, the calcination area and the preheating area.

The key element in this calciner (and its first major advantage) is the vibrating table used to convey the material from the limestone feed-in to the CaO outlet. This allows for a controlled residence time which is critical for the full completion of the reaction, without dependence on a free fall particle. It also ensures homogeneous thickness distribution of the material across the table due to the vibration. The speed at which the particles travel is directly related with the frequency and amplitude of the vibration. This can be adjusted for different particle sizes, giving flexibility for testing several materials.

The reflected beam from the secondary concentrator enters into a cavity with reflective walls and an absorptive bottom, which receives most of the thermal power. The bottom plate material in turn transfers the heat into the calciner furnace under the plate, by pure conduction within the plate and by radiation and convection on the lower side.

And this is the second major advantage of this design: using a proper material for the bottom plate, a homogeneous temperature distribution is achieved even under non-homogeneous solar flux, due to the internal thermal conductivity of the plate. This material should have two key properties: a good thermal conductivity, and high absorptivity and emissivity in order to absorb the incident solar flux and re-radiate the thermal power to the underlying solar furnace. A good temperature distribution combined with the even thickness of the material layer on the vibrating table and the mixing of the particles due to the vibration ensures a controlled and homogeneous reaction.

Given that the geometry is very simple (a squared flat plate with constant thickness), any material could be adapted for this purpose. In particular, silicon carbide is a good candidate as it is able to withstand very high temperatures and has the desired physical properties described above.

The solar calciner presents several challenges at large-scale that will be analysed at SOCRATCES prototype, namely: i) transfer losses in the high-temperature solar receiver, particularly re-radiation losses; ii) heat transfer to particles by radiation; iii) thermal gradient between particles; iv) difficulty to control flux profile across reactor; v) beam-down technology performance in terms of solar flux distribution along the receiver; vi) thermomechanical stresses induced on the solar receiver. For more information see the document *“Downscale study of the proposed full scale SOCRATCES plant”.*

2. SOLAR RECEIVER GEOMETRY AND LOCATION (ST3.4.1)

The solar receiver is composed of a primary reflector (heliostat field), a secondary reflector (re-concentrator) and a cavity where the solar irradiation is converted into usable heat and transferred to the calciner reactor where the calcination reaction takes place. The calciner reactor is situated on the top of a tower just below the secondary reflector, see Figure 2.1, where a complete scheme of the solar receiver system is presented in 3D CAD.

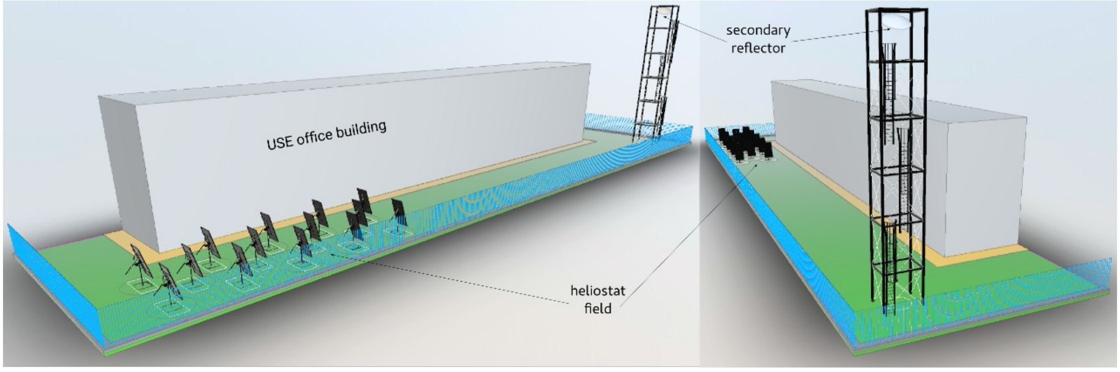

Figure 2.1. General view of the project plot with solar receiver: primary (heliostat field) and secondary (beam-down re-concentrator) receivers.

The different parts of the solar receiver are now described in detail.

2.1. Primary reflector: Heliostat field

The heliostat is a drive mechanism that moves a mirror mounted on a two axes orientable structure so that the reflected beam is directed to the desired target. The orientation is changing dynamically with the sun apparent motion to maintain a static target.

Figure 2.2. Mirror mounted on the heliostat.

Figure 2.3. Heliostat mechanism with linear drives.

Several of these heliostats are arranged to increase the concentration of the solar power in the receiver, forming the so-called heliostat field.

2.1.1. Heliostat selection

For this project a commercial, off-the-shelf heliostat has been selected. There are several reasons for this decision:

- The purpose of Socratces is not to design a new heliostat.
- A new design would require a lot of effort in terms of time and cost, and for a small number of heliostats it doesn't pay off.
- Commercial heliostats are readily available in case of maintenance or replacing parts, which are not custom made.
- If extra solar power is needed, more heliostats can be procured in a short time.

The criteria followed in the search for an adequate heliostat has been:

1. Price: the heliostat should cost a reasonable amount even for small quantities. Typically, the cost of a heliostat is considered on a price per square meter of reflective surface for comparison purposes.
2. Country of origin: a European based supplier is preferred to avoid custom charges and paperwork, such as Value Added Taxes management and other issues like warranties, etc. Also, it is in the spirit of the European Commission programme to benefit European partners and companies given that the funding comes from European taxpayers.
3. Technical performance: factors such as mirror size, reflectivity, accuracy, movement range, power controllers, communication protocols, etc. are crucial for the validity of a heliostat.
4. Endurance: the structure, materials, coatings, etc. must withstand an outdoors installation, and the highest wind foreseen by the local regulations.
5. Availability: having the heliostats readily available is an advantage given the tight time constraints of the project.

All in all, a supplier has been found that hits a sweet point in all of these fields. A single unit has been procured and installed for testing and characterization purposes.

2.1.2. Heliostat field design process

The boundary conditions for the solar field design are the 15 to 20 kW thermal power required at the receiver, the size, shape and orientation of the plot available, and the height of the tower which is determined by the equipment (reactors).

The first design criteria comes from the fact that we need a very high temperature with a relatively low incident power. Thus, a high concentration within a small aperture in the receiver is needed to keep thermal losses low. Therefore, a secondary concentrator is needed on top of the receiver in a beam down configuration, and that concentrator imposes some design restrictions on the heliostat field.

Given that the heliostats don't need to concentrate by themselves, the mirror can be flat which lowers the cost and avoid having to specify the curvature or focal length. This also reduces optic aberration for a non-perpendicular solar incidence angle.

Having a single parabolic concentrator, which has a single focal point, means that only rays of light parallel to the parabola axis are concentrated into the focal point. Rays coming from different heliostats will not be parallel and therefore their reflected beams will be out of focus. This fact translates into a scattered collection of beam shapes, each one of them corresponding to a single heliostat. The greater the distance between heliostats, the bigger the aperture of the receiver in order to let all the flux penetrate the receiver cavity. This leads to bigger losses through the aperture.

The only way to minimize this effect is to pack the heliostats as close as possible, so the solid angle seen from the secondary reflector is smaller, and to have the group of heliostats as far as possible from the tower. The latter condition is easily implemented by start placing heliostats at the limit of the plot, and adding more units closer to the tower. But the former condition (reducing the distance between heliostats) have a consequence on the performance of the solar field, because blocking and shadowing effects increases.

So, the number and layout of heliostats is a compromise between overall performance of the solar field and size of the aperture window at the receiver. The procedure is iterative, starting with a distribution that minimizes the blocking and shadowing losses, and checking for the received power and aperture size. This process is performed with the sun at an arbitrary position since there is no need for a sunrise to sunset commercial operation, in which the objective is to maximize the total energy annually.

2.2. Secondary reflector: Beam-down re-concentrator

While Atria was involved in the project, a first approach to the secondary reflector was studied. It was based on a low cost off-the-shelf parabolic offset antenna with a reflective coating similar to a chrome plating. The parabola shape is a good choice for the secondary reflector, provided it is well positioned between the heliostat field and the cavity receiver aperture focus, and provided the coating performs with good solar reflective properties.

A picture of the parabolic antenna (without the reflective coating) is presented in Figure 2.4. We call this model *Secondary Reflector 1* (SR1).

When Atria withdrew and Virtualmech started working on the project, new options were available. Virtualmech had been working with a manufacturer of low cost thermal CSP components based on Parabolic Dish for medium temperature applications. Figure 2.5 presents details of the original application of the mirrors, configured in groups of four facets to build up the parabolic dish. Figure 2.6 presents CAD views of the single mirror with exact geometry. Optical and geometrical properties of the system are given in Appendix A.

With the mirrors available, an arrangement for the secondary reflector can be carried out to improve performance and arrive to an optimum. This arrangement is called from now on *Secondary Reflector 2* (SR2). In any case, the solar reflectivity of the parabolic antenna after the chromed plate treatment shouldn't be very high, a maximum of R_{SR1} = 83% is envisioned, with expected slope and specularity errors much higher than those of the mirrors-based system SR2, with reflectivity of the order of R_{SR2} = 95%, which provides 12% more energy to the receiver. Both models have been tested at the raytracings carried out in ST4.3.4.4. Solar Flux Simulation (Section 5).

Figure 2.4. Parabolic dish antenna to be used in SR1, without the mirror coating.

Figure 2.5. Parabolic mirror for SR2.

Figure 2.6. Parabolic dish from third party. Mirrors used for secondary reflector of SOCRATCES. Images provided by Thermal Cooling Technology S.L. and reproduced with permission. Mirrors used in SR2.

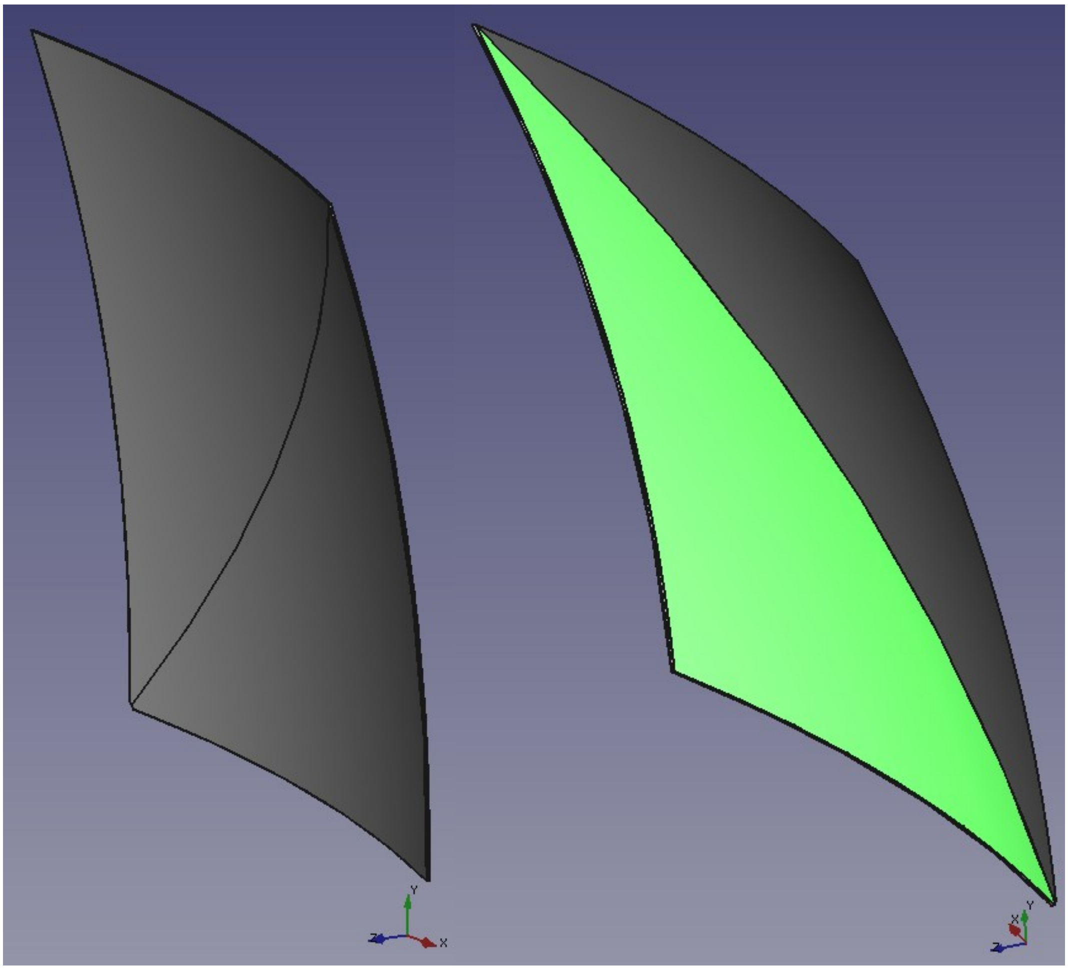

Figure 2.7. CAD view of single facet. Used as building blocks of SOCRATCES' own secondary reflector SR2.

Comparing both approaches, the following can be stated:

- SR2 facets is cheaper than SR1 dish+coating
- SR2 has better optical properties than SR1, with 12% more reflected energy for the former
- SR2 optical errors are (expectedly) lower than those of SR1, nevertheless given the small distance between the concentrator and the receiver, this should be of no importance.
- SR1 is made of just one piece and with the fittings included to install on a mast, therefore installation and supporting structure should be easier and cheaper
- On the other hand, SR2 supporting structure is more complex and expensive but allows the design of a mobile-adaptable system that can be fine-tuned easily and can have different configurations for different seasons of the year and even time of the day, if in the future the supporting structure were to be automated so that its shape can be transformed by system control

Solution SR2 seems superior to SR1, but this should be stated once raytracings are performed and comparisons between both approaches are carried out in ST3.4.4.

3. SOLAR RECEIVER MATERIAL PROPERTIES (ST3.4.2)

3.1. Primary reflector: Heliostat mirror

The heliostat mirror consists of a flat composite sandwich with the following properties (see Annex C for full datasheet):

- Reflective anodized aluminum side, highly polished with transparent epoxi coating. Total solar reflectivity is 88% (ASTM 891-87) and specular solar reflectivity is 83% (DIN 5036-3, ASTM E-1651).
- Core made of polyethylene LDPE (0,92 gr/cm3).
- Back side of aluminum mill.

This sandwich mirror is mounted on an aluminum frame which in turn is attached to the tracking mechanism.

3.2. Secondary reflector SR1: parabolic antenna

The parabolic dish is an offset antenna made of galvanized steel with an epoxi coating. The dish is supported by a secondary frame with is attached to the mast.

The concave side of the parabolic dish is painted with a highly reflective coating similar to a mirror.

3.3. Secondary reflector SR2: mirrors arrangement

The facets of the SR2 are manufactured by Rioglass, and are made of flat annealed glass, with a silver coating with a reflectivity between 93,5%-95%, and a precision better than 1 mrad total RMS.

Behind the silver layer, a copper layer and three paint layers provides environmental protection.

3.4. Indirect CFC Solar Calciner (ICFC-SC)

The ICFC-SC solar calciner system has been proposed by CLX where the material used is a special stainless steel. These steels are designed for high temperature applications with a good resistance to oxidation in the relevant temperature range. Their properties are used in FEM models of CLX solar calciner system in order to accurately reproduce the thermal and mechanical real behavior of this component. Special attention has been addressed to radiative properties due to its importance in Solar Raytracing and thermal-mechanical models, where input and output solar power are key issues in the development of this project. There are three main parameters that have been studied:

- Normal Total Emittance
- Normal Solar Reflectance
- Normal Solar Absorptance

These properties have been extracted from a TPRC Data Series [1], thermal and radiative properties from stainless steels have been selected and then averaged in order to fully represent the behavior of the present material. Several cases of stainless steel and conditions have been studied and then compared to obtain the finally used, indicative, properties.

3.5. Indirect Cavity SiC Solar Calciner (ICSiC-SC)

In the ICSiC-SC calciner cavity there are two areas with different purposes: reflection and absorption of the solar radiation. The objective of the cavity is to direct the solar power to the Silicon Carbide bottom, where it is absorbed and transferred to the calcination area under the SiC plate. Therefore, the walls should reflect solar power and avoid absorbing heat.

- Bottom side: made of SiC.
- Walls and top side: made of a sandwich of several layers
    - The inside layer is made of Promat Scuttherm® LT HW, which has excellent reflectivity and low absorptivity properties.
    - The intermediate layer is made of Promat Microtherm® Panel-1000R, which has low thermal conductance.
    - The outer layer is made of EN 1.4301 steel, to provide a supporting frame for the panel and also to prevent water ingress.

4. HELIOSTAT CHARACTERIZATION (ST3.4.3)

Once selected a valid heliostat with the criteria followed in section 2.1.1, and having a test unit installed on the roof of the Higher Technical School of Engineering, it is necessary to perform a series of tests in order to validate the heliostat and also to measure some operational parameters needed for the simulations of the complete solar field.

4.1. Kinematics and motion range

A conventional heliostat moves in two axes, typically azimuth and elevation. This is the kinematics chosen by the majority of commercial CSP plants with heliostats, and fits very well with the polar coordinate system used for the solar position and the reflected beam calculations.

Our chosen heliostat however does not use the azimuth-elevation kinematics, but a different one named elevation-hour angle (or pitch-roll). It has the advantage of a simple motion by using two linear actuators, but at the cost of more complex equations and a limited motion range on the hour angle axis.

For the elevation axis, the range varies from 15º to 90º.

For the hour angle axis, the range varies from -50º to 50º.

This limited range for the hour angle axis makes necessary a careful selection of the position in which the heliostat will be mounted, in order maximize the solar tracking.

There is a need to translate a linear position of the two actuators into an angle of the heliostat mirror. This could be done by measuring the geometry, and performing the translation with a direct kinematic.

4.2. Mirror characterization

The mirror size has been measured to check the compliance with the data sheets, having found a good agreement between both.

The flatness of the mirror surface has been visually checked by observing the reflected beam at a long distance. Due to the sun shape, the reflected beam should be seen as a round disc if there is no distortion. During several moments of the day, this reflected shape has been pictured at long distances (about one order of magnitude compared with the distance to be used at Socratces) with a good similarity with the theoretical result.

Mirror reflectivity has not been checked due to the lack of the appropriate measurement instrument, so and indirect measuring method will have to be devised such as comparing incident and reflected irradiation with a pyrheliometer.

4.3. Linear actuators accuracy and repeatability

The manufacturer claims an accuracy of the heliostat of +/-0,1 degree. For the characterization of this parameter, the repeatability has been taken instead because it is more important for the performance of the heliostat. The accuracy can be adjusted later by calculating a correction curve based on the readings of an absolute inclinometer.

Both axes have been taken to the most unfavorable position. For the elevation axis, that corresponds to the minimum elevation (15º), in which a given increase of the linear actuator translates into a maximum angular deviation. By comparing the position of a corner of the mirror against a fixed reference and moving back and forth several times the elevation axis, the observed error does not exceed the +/-2 mm in absolute position which is the distance corresponding to the 0,1º.

For the hour angle axis, the worst scenario is 50º west, and the tolerance is +/-1 mm.

All the tests must be performed with several homing procedures, to take into account the sensitivity of the limit switch and not only the incremental encoder.

4.4.Local controller

The local controller is the equipment in charge of commanding the linear actuators, read the heliostat position and communicating with the solar field controller. Therefore, it will have a high-power stage to supply enough current to the electrical motors, and a low power stage for signaling and communications.

In order to characterize the local controller, the following points must be considered:

- Current absorbed: necessary to calculate the cross section of the power cables, following the low voltage regulations. The supplier states a maximum of 2,5 A.
- Encoders: to avoid losing the position, encoders should be used to close the feedback control. I.e., open loop stepper motors should be avoided as there is no guarantee that any step is lost. This heliostat uses brushed DC motors with incremental hall encoders, and therefore the actual read position is reliable. It has the inconvenience that a homing (fully contracting of the actuator until a physical switch is activated) is necessary on every power-up as the incremental counter is lost when the power supply is switched off.
- Communications: the protocol and memory maps must be available for communication of several heliostats with the solar field controller. A standard protocol should be used for compatibility with third party controller. In our heliostat, a Modbus RTU under RS485 is used, and the memory map has been made available, thus making possible full communication between the heliostats and the main controller. Moreover, this local controller is capable of performing the solar vector calculations and automated tracking of a target, although those features will not be used.
- Alarms: the heliostat must give an alarm in case of malfunction so that the solar field controller can take appropriate actions. The following failures must be detected: drive cable disconnected, high current trip, mechanical blockage of the actuator.
- Enclosure: the local controller must be installed inside a weatherproof casing, so that rain or dust does not affect its performance. Also, the cabling must be according to the size of the cable glands to avoid water ingress.

All of the above have been checked and validated for our purposes.

5. SOLAR FLUX SIMULATION (ST3.4.4)

Once the heliostat, cavity solar receiver and concentrator have been selected, it is time to simulate the solar field with a raytracing software in order to obtain the solar flux maps inside the cavity and feed the thermal-mechanical model exposed in Section 6. The raytracing software used in this project is SolTrace [Web 1], which is an open-source software tool developed by the National Renewable Energy Laboratory (NREL) to model CSP systems and analyze their optical performance. At the beginning of this project, this part was provided by Atria by obtaining an initial model shown in Figure 5.1. This model has 14 heliostats positioned from 50 to 70 meters far from the tower, a paraboloid concentrator with a protection screen in front of it in order to protect the steel structure, and a planar surface of 200x200mm as the receiver.

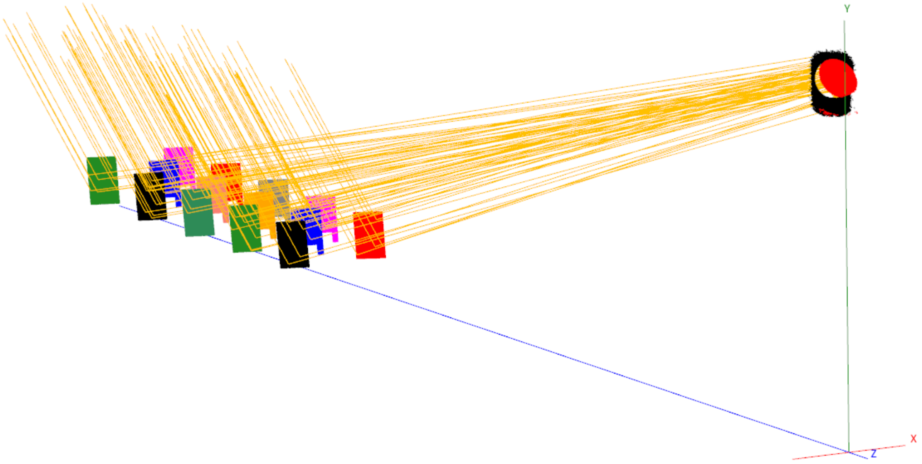

Figure 5.1. Raytracing initial model provided by Atria.

The position of the sun for this model was represented approximately as a random day when the sun has its highest altitude. Due to the preliminary state of this phase when it was made, the position of the sun was not important nor determined for the aim of the project. At this stage, the input power to the receiver was around 19 kW, considering the sun shape and including small optical errors. In Figure 5.2, the flux map at the planar receiver is shown, where it can be found that most of the rays incoming to the surface are concentrated in one point with high flux intensity around 4 MW/m². This flux map was not simulated in a thermal-mechanical model.

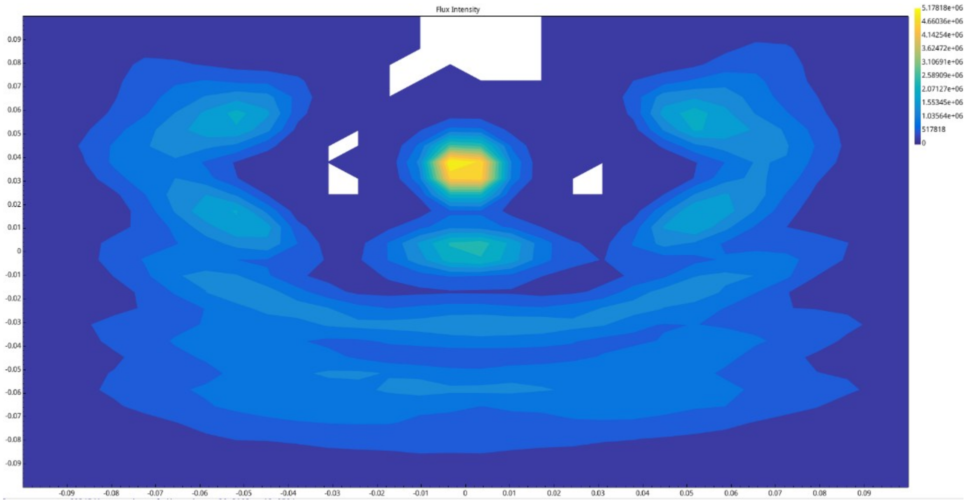

Figure 5.2. Flux map [W/m²] at the square receiver of the initial model provided by Atria.

The first model developed by Virtualmech is shown in Figure 5.3, where the sun position is the equivalent to the 21st of June at 14:30 exactly at the coordinates of the project mentioned in Section 1. In addition, the sun shape chosen is a Pillbox with 4.65 mrad of angle from center. The heliostat field axis is turned 18° west compared to the north (Z axis in Figure 5.3), and the number of heliostats is the same as previous assumptions of Atria, I.e., 14. The protection screen was removed in order to implement in an easier way the new geometries of solar cavities. The diameter of the paraboloid concentrator was changed to 2 meters in order to reproduce the offset-parabola shown in Figure 2.4, and the relative position of the cavity entry and the concentrator was optimized by iterating with the input power to the cavity walls.

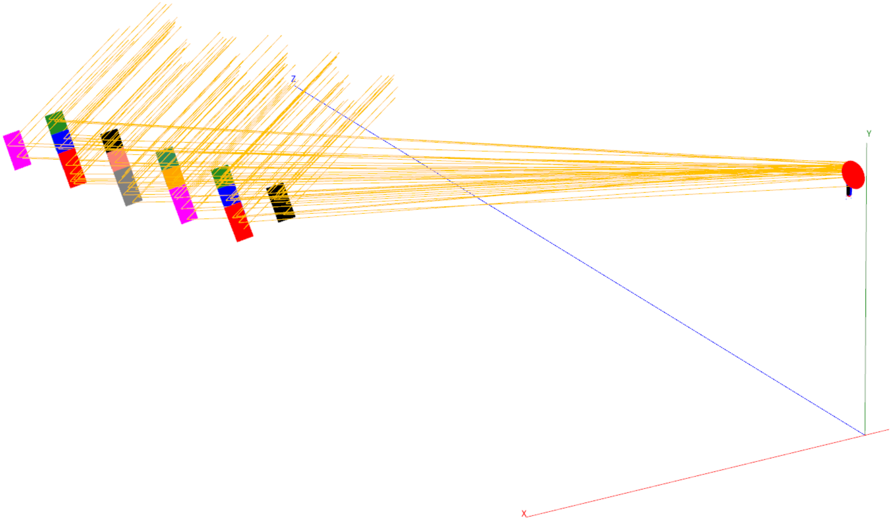

Figure 5.2. Heliostat field of the Model V01 of Virtualmech.

The second and current version of the system is shown in Figure 5.3, where the protection screen for the steel structure is included, and a protection screen for cavity is also included (colour blue in Figure 5.4 and orange in Figure 5.5). The purpose of this new screen is to avoid concentrated rays hitting on the external surface of the receiver. In this model, some virtual surfaces for postprocessing purposes have also been included in the concentrator and receiver entry. For instance, in Figure 5.5 is shown the flux map on a virtual surface on the entry of both cavities analysed.

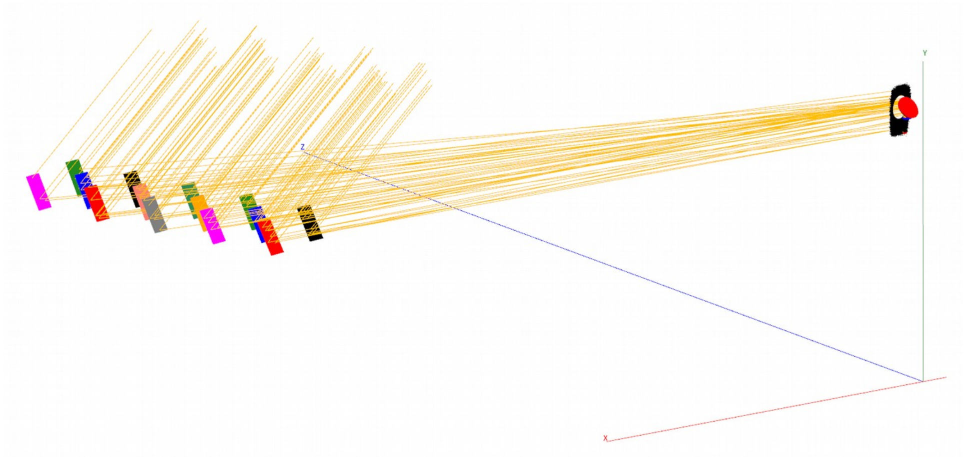

Figure 5.3. Heliostat field of the Model V02 of Virtualmech.

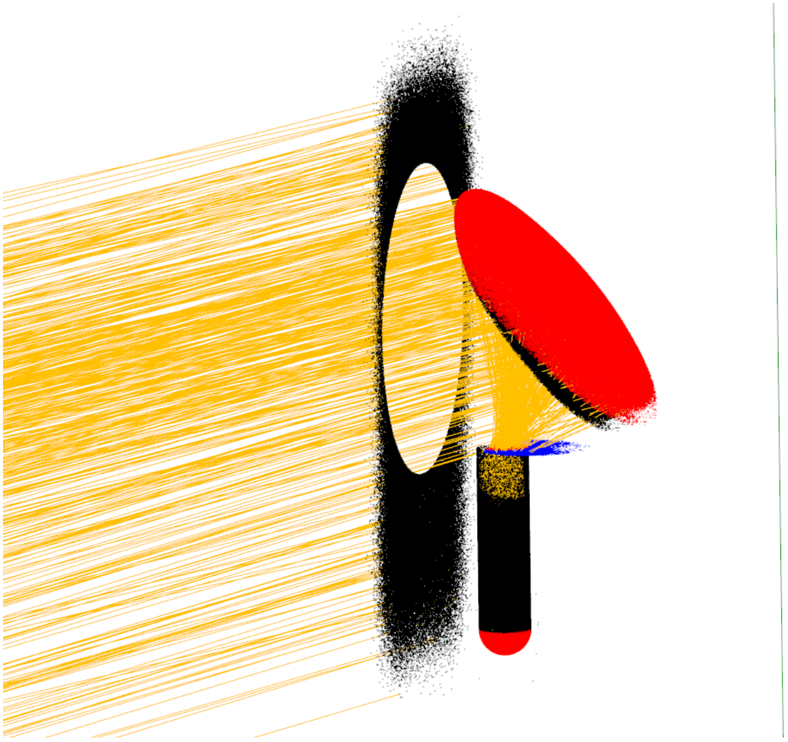

Figure 5.4. Protection screen, concentrator and Indirect CFC Solar Calciner of the Model V02 of Virtualmech.

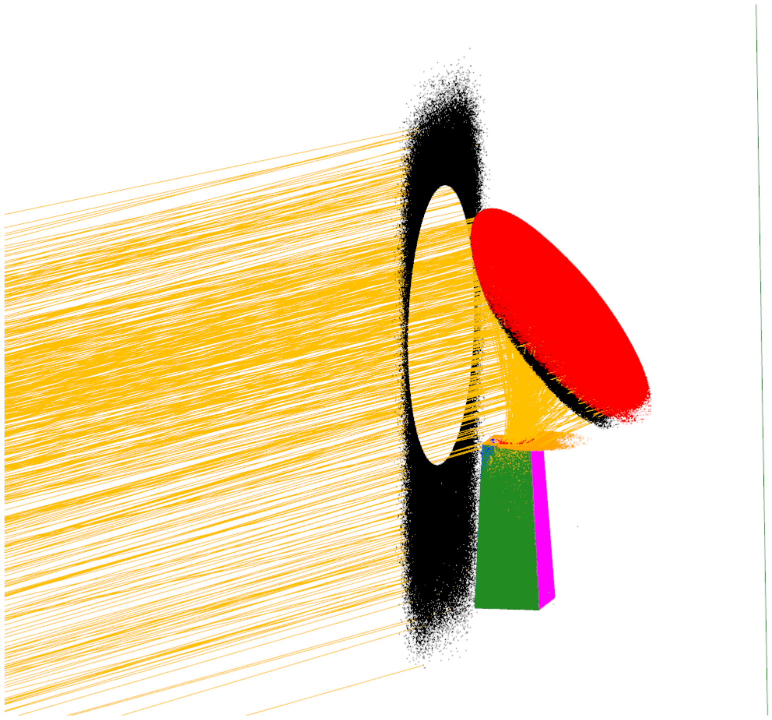

Figure 5.5. Protection screen, concentrator and Indirect Cavity SiC Solar Calciner of the Model V02 of Virtualmech.

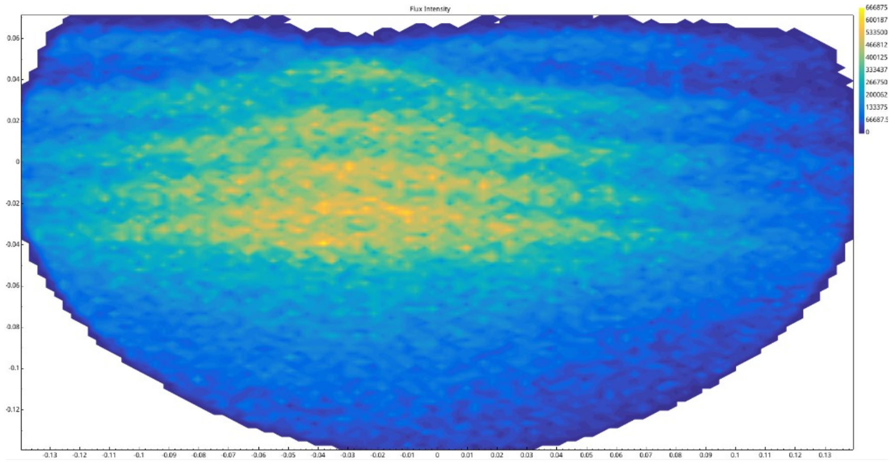

Figure 5.6. Flux map [W/m²] at the entrance of the cavities of the Model V02 of Virtualmech.

5.1. Indirect CFC Solar Calciner

This cavity is composed by a cylinder with one side open and the other closed by a semi-sphere, detailed information is provided in Section 6. Once the heliostat field, concentrator and cavity geometry and position have been obtained, a study regarding the thermal and optical radiative properties of the inner surface of the stainless steel cavity has been carried out.

The following cases have been simulated:

- Original material: (stainless steel) - Case 7 according to Figure 5.7
- Original material with same reflectance as heliostat: Case 8 according to Figure 5.7.
- Original material with Pyromark painted inside the cavity: Case 9 according to Figure 5.7 (properties of Pyromark shown in Figure 5.9).
- Original material but Oxidized: Case 10 according to Figure 5.7.

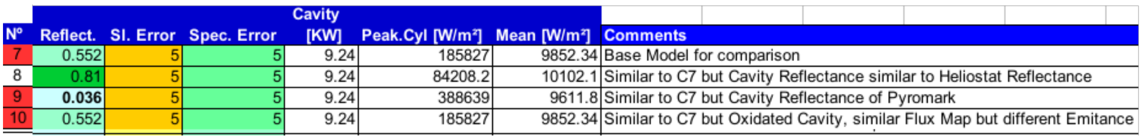

Nº	Reflect.	Sl. Error	Spec. Error	Cavity [KW]	Peak.Cyl [W/m²]	Mean [W/m²]	Comments
7	0.552	5	5	9.24	185827	9852.34	Base Model for comparison
8	0.81	5	5	9.24	84208.2	10102.1	Similar to C7 but Cavity Reflectance similar to Heliostat Reflectance
9	**0.036**	5	5	9.24	388639	9611.8	Similar to C7 but Cavity Reflectance of Pyromark
10	0.552	5	5	9.24	185827	9852.34	Similar to C7 but Oxidated Cavity, similar Flux Map but different Emitance

Figure 5.7. Cases of study of different reflectance of the inner surface of the receiver.

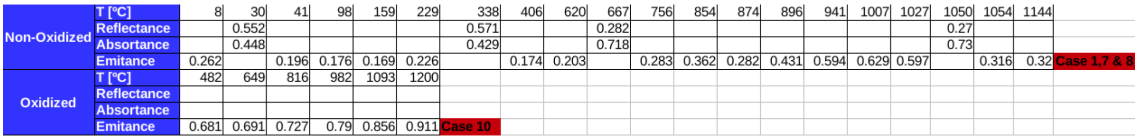

Non-Oxidized	T [ºC]	8	30	41	98	159	229	338	406	620	667	756	854	874	896	941	1007	1027	1050	1054	1144	
	Reflectance		0.552					0.571			0.282								0.27			
	Absortance		0.448					0.429			0.718								0.73			
	Emitance	0.262		0.196	0.176	0.169	0.226		0.174	0.203		0.283	0.362	0.282	0.431	0.594	0.629	0.597		0.316	0.32	Case 1,7 & 8
Oxidized	T [ºC]	482	649	816	982	1093	1200															
	Reflectance																					
	Absortance																					
	Emitance	0.681	0.691	0.727	0.79	0.856	0.911	Case 10														

Figure 5.8. Thermal and Optical radiative properties for non-oxidized and oxidized states of the inner surface of the cavity as a function of temperature.

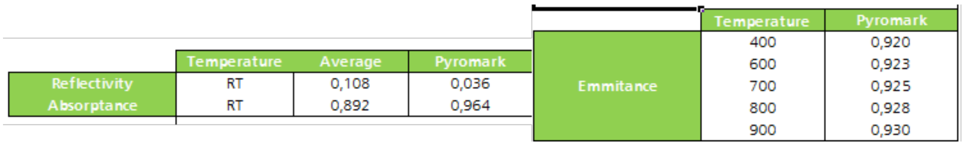

	Temperature	Average	Pyromark
Reflectivity	RT	0,108	0,036
Absorptance	RT	0,892	0,964

	Temperature	Pyromark
Emmitance	400	0,920
	600	0,923
	700	0,925
	800	0,928
	900	0,930

Figure 5.9. Thermal and Optical radiative properties for Case 9 (figure 5.7): Pyromark painted on the inner surface of the cavity as a function of temperature.

These four cases have been simulated in SolTrace and then flux map on the inner surface have been exported to thermal-mechanical simulations shown in Section 6. Regarding optical performance knowing that these cases have the same input power from the concentrator, some conclusions have been extracted:

- High values of reflectance generate more uniformity in flux maps and, therefore, more uniformity in temperature fields as shown in Figure 6.15. This result is convenient for the top side of the cavity where the peak of flux is located.
- Low values of reflectance increase peak flux due to the high absorptance, I.e., most of the energy is absorbed by the receiver instead of reflected and the high gradient of temperature due to the concentration or rays coming from the paraboloid is not avoided.
- Thermal effects due to emittance changes are provided in Section 6.
- The optimal solution for the problem of high temperature gradients due to high concentration of rays coming from the concentrator is to have a high reflectance on the top side of the cavity and paint with Pyromark the rest of the cavity. With this, high gradients of temperatures (therefore, high stresses) are avoided, and then on the bottom of the cavity, the high absorptance generates a homogeneous flux map.

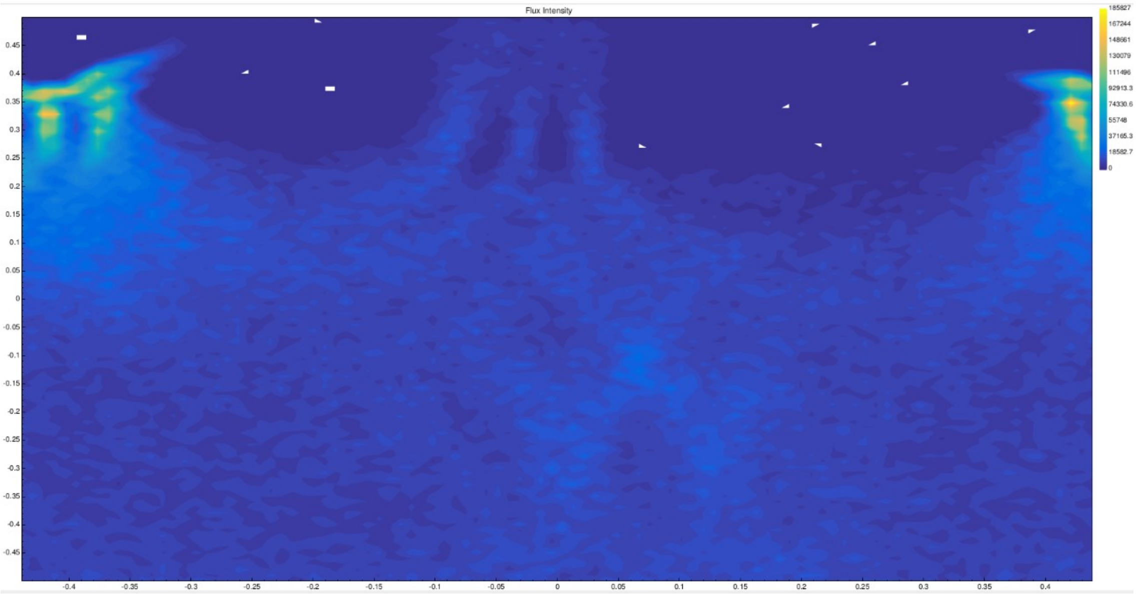

Figure 5.10. Flux map [W/m²] on the inner surface of the receiver (cylinder) for Case 7 (according to Figure 5.7). Peak Flux of 186 [kW/m²] is obtained.

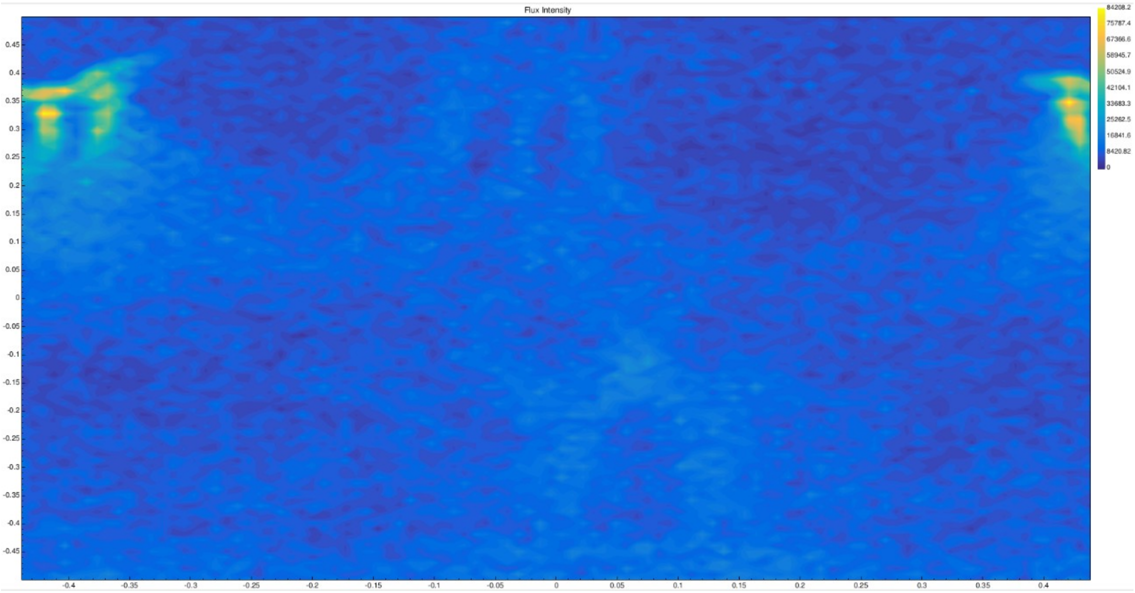

Figure 5.11. Flux map [W/m²] on the inner surface of the receiver (cylinder) for Case 8 (according to Figure 5.7). Peak Flux of 84 [kW/m²] is obtained.

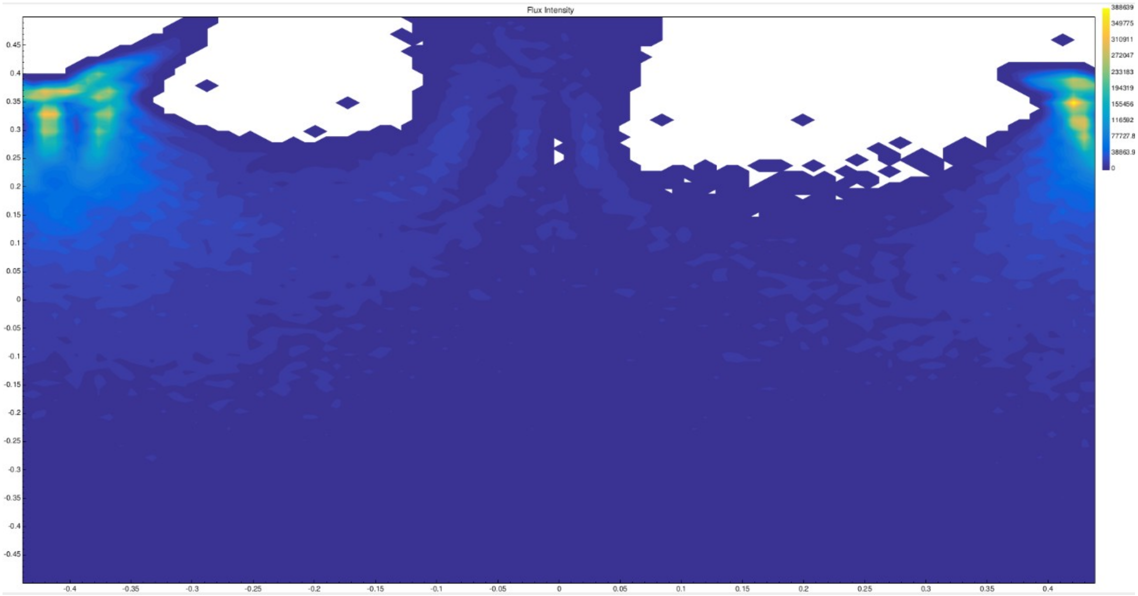

Figure 5.12. Flux map [W/m²] on the inner surface of the receiver (cylinder) for Case 9 and 10 (according to Figure 5.7). Peak Flux of 388 [kW/m²] is obtained.

5.2. Indirect Cavity SiC Solar Calciner

This receiver is characterized by 5 inner faces forming a truncated pyramid with an opened top side where the concentrated rays enter the cavity. Despite CLX cavity where the optical error type inside the cavity is Gaussian, in this cavity the error type is diffuse due to the radiative properties of the Scuttherm. As seen in Figure 5.13, the most affected surface by the rays is Surface 3. The optimal results would be to concentrate most of the incoming rays on Surface 1 where the output power of the system is quantified. The next steps to be done is to increase the input power to Surface 1 and decrease the thermal gradient on all surface in order to also reduce high stresses caused by these thermal expansions.

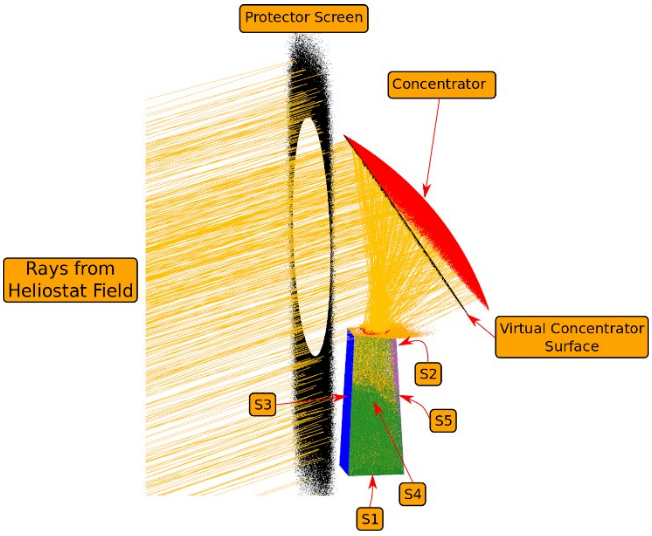

Figure 5.13. Description of the nomenclature for inner surfaces of USE receiver.

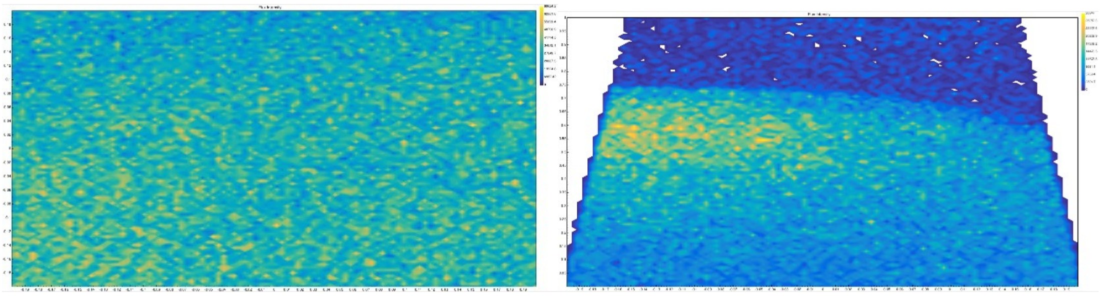

Figure 5.14. Flux map [W/m²] on the inner surface S1 and S2 of the USE receiver. Peak Flux of 70 and 29 [kW/m²] respectively are obtained.

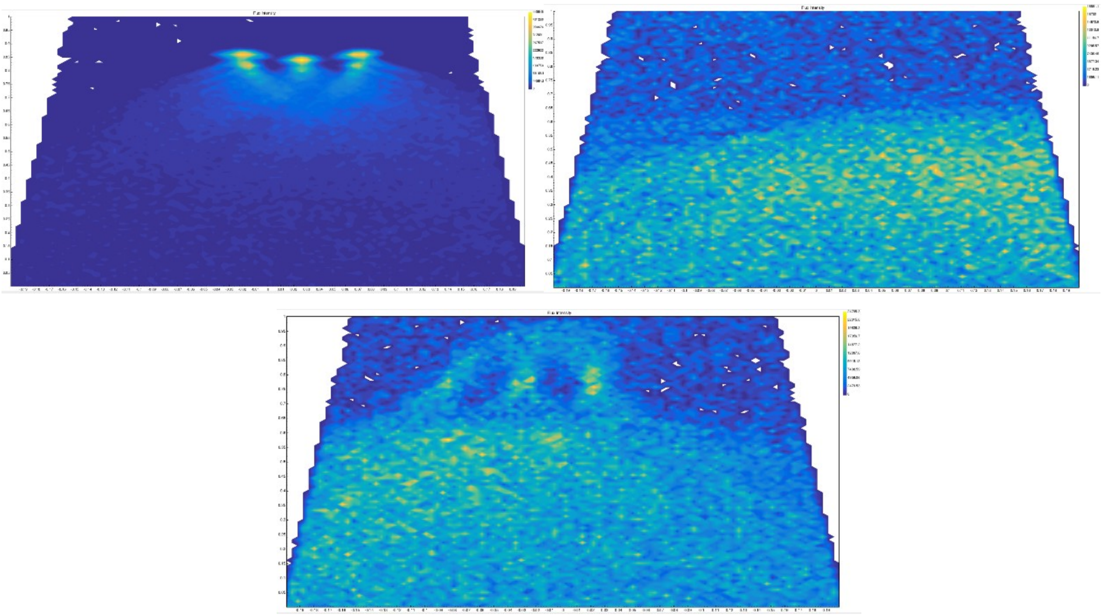

Figure 5.15. Flux map [W/m²] on the inner surface S3, S4 and S5 of the USE receiver. Peak Flux of 446, 29 and 25 [kW/m²] respectively are obtained.

5.3. Slope and Specularity Error study

The purpose of this study has been to analyze the importance of the slope and specularity error of the reflective surfaces of the system (heliostat, concentrator, and cavity), in the input power of the different stages. Case 1 is the base model where errors of heliostat, concentrator and cavity are low (cavity is not designed for good errors, therefore, 5 mrad of slope and specularity error are considered as low). In Figure 5.16 is shown the 6 different cases with the input power of each stage [kW], and the peak and mean heat flux on the inner side of the cavity. In this study, only CLX receiver has been considered.

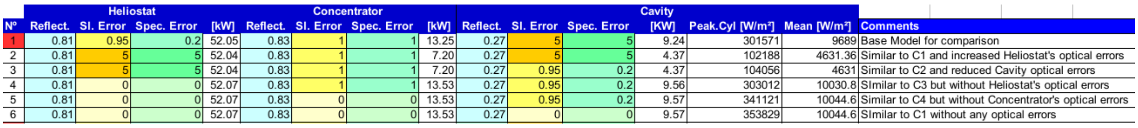

	Heliostat				Concentrator				Cavity						
Nº	Reflect.	Sl. Error	Spec. Error	[kW]	Reflect.	Sl. Error	Spec. Error	[kW]	Reflect.	Sl. Error	Spec. Error	[KW]	Peak.Cyl [W/m²]	Mean [W/m²]	Comments
1	0.81	0.95	0.2	52.05	0.83	1	1	13.25	0.27	5	5	9.24	301571	9689	Base Model for comparison
2	0.81	5	5	52.04	0.83	1	1	7.20	0.27	5	5	4.37	102188	4631.36	Similar to C1 and increased Heliostat's optical errors
3	0.81	5	5	52.04	0.83	1	1	7.20	0.27	0.95	0.2	4.37	104056	4631	Similar to C2 and reduced Cavity optical errors
4	0.81	0	0	52.07	0.83	1	1	13.53	0.27	0.95	0.2	9.56	303012	10030.8	SImilar to C3 but without Heliostat's optical errors
5	0.81	0	0	52.07	0.83	0	0	13.53	0.27	0.95	0.2	9.57	341121	10044.6	Similar to C4 but without Concentrator's optical errors
6	0.81	0	0	52.07	0.83	0	0	13.53	0.27	0	0	9.57	353829	10044.6	SImilar to C1 without any optical errors

Figure 5.16. Cases of study of slope and specularity error.

From this study, some conclusions have been extracted:

- By comparing Cases 1 and 2, it can be extracted that errors on the heliostat surface have a great influence on the input power of the concentrator and, as a consequence, the input power to the receiver. This is because the big distance (50 to 70 meters) between the heliostat field and the concentrator. Small variations of slope and specularity errors fall into great variations on the optical performance of the system. Therefore, due to the lack of data on this matter (heliostat datasheet does not provide this information), it is very important to characterize these errors in order to obtain accurate results from the raytracing model.
- By comparing Cases 4 and 5, it can be extracted that errors on the concentrator have a low influence on the input power to the receiver due to the relatively small distance between these two components.
- By comparing Cases 2 and 3, or 5 and 6, it can be extracted that errors on the inner surface of the receiver have a low influence on the input power to the receiver because no additional radiation exits the receiver due to its small confinement. Therefore, optical errors due to inner surface receiver irregularities are not important for the performance of the system.

6. SOLAR POWER TO CALCINER SIMULATION (ST3.4.5)

As stated above, two different solar calciner configurations have been studied, Finite Element Modeling (FEM) technique has been employed for this purpose. Both thermal and structural analyses have been carried out for the Indirect CFC Solar Calciner. As for the Indirect Cavity SiC Solar Calciner, only a thermal model has been done. All models built so far are stationary.

The aim of the thermal models is to get the heat flux that the solar field can provide for the calcination reaction, considering all losses related to the thermal problem, and therefore a global efficiency is calculated for each case studied. The temperature field in all solids studied is obtained as well.

Structural models take into account the temperature field provided by the thermal analyses and adds the mechanical restrictions imposed by the continuity of surrounding parts. The stress field in all solids studied are calculated.

A brief description of the FEM process will be presented as follows.

6.1. Indirect CFC Solar Calciner

6.1.1. Geometry Model

Figure 6.1 depicts the whole calciner 3D geometry provided by CLX, showing a zoom at the Indirect CFC Solar Calciner. The only parts of interests for the present sub task are the solar receiver and the shell surrounding it, shown in red and blue respectively. They together form the solar reactor annulus where the limestone particles cloud chemical reaction takes place. Figure 6.2 shows both parts and the reactor annulus within.

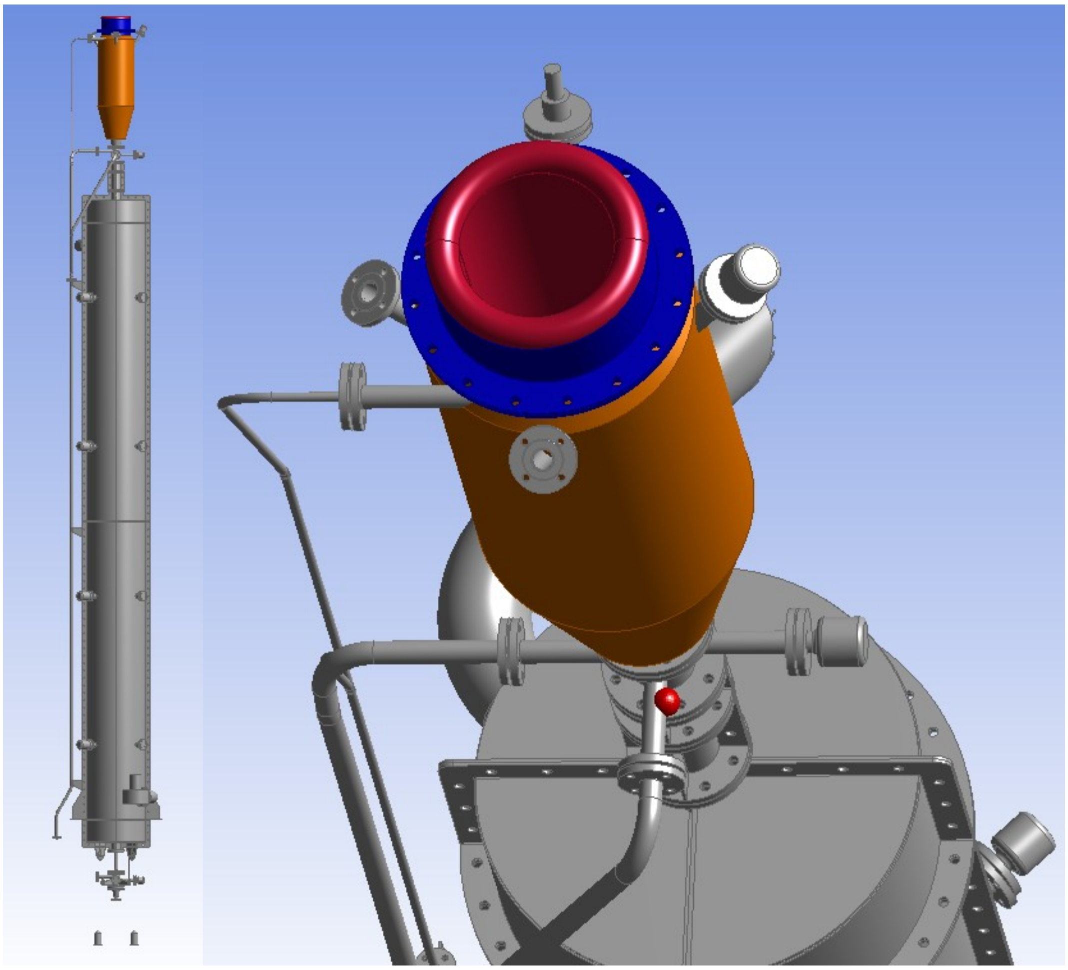

Figure 6.1. Calciner geometry.

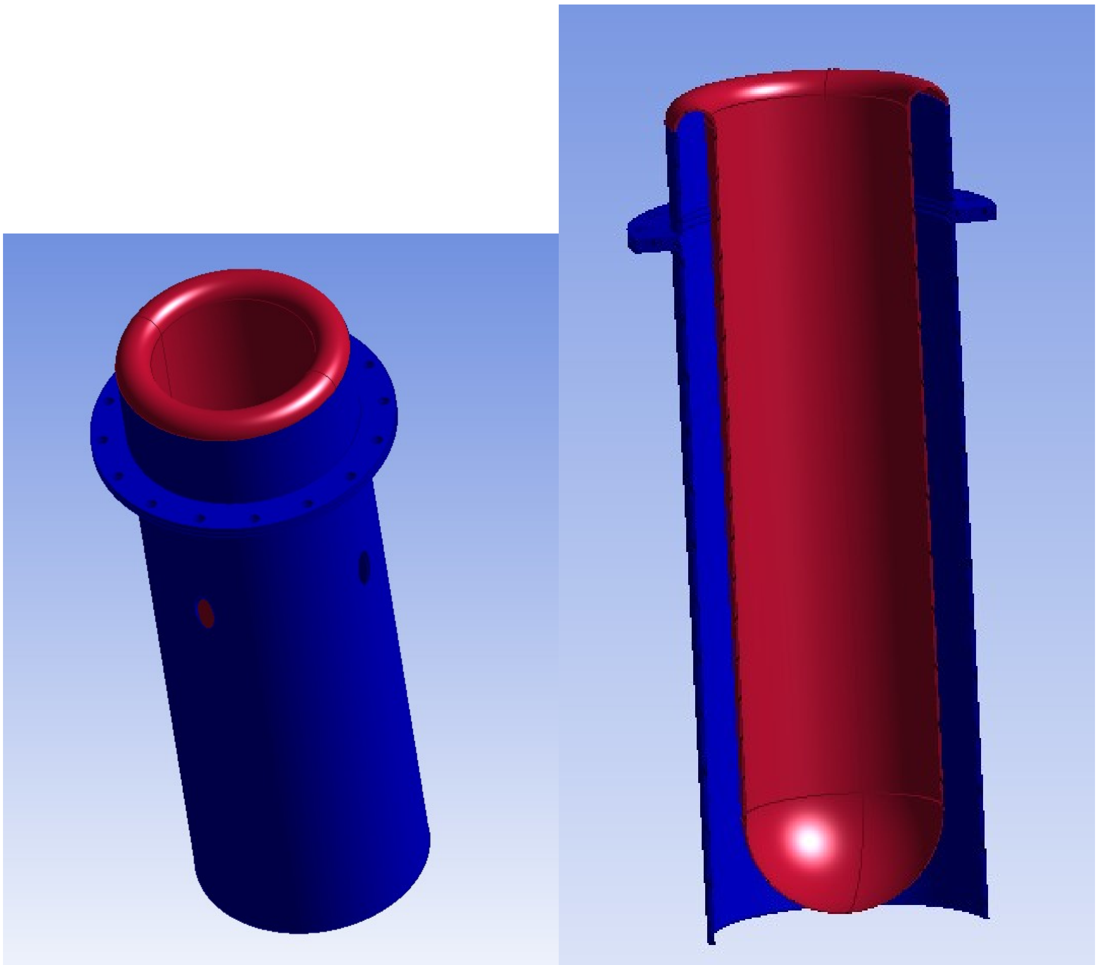

Figure 6.2. Solar receiver and outer shell forming the reactor annulus.

Some modifications to the original geometry have been done in order to simplify the models:

- The isolating material covering the reactor shown in orange in Figure 6.1 is removed
- The reactor annulus is closed by closing the shell surrounding the solar receiver at the bottom, by adding a solid parallel to the solar receiver shape, as shown in Figure 6.3

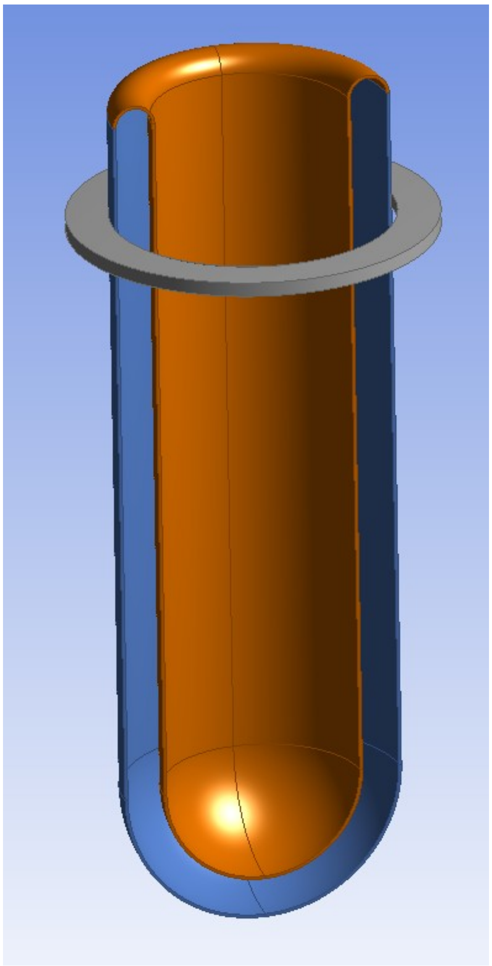

Figure 6.3. Simplified geometry.

6.1.2. Meshing

Once the geometry model is defined, it is passed to a mesh module in order to build the Finite Element Model in terms of nodes and elements.

All domain is discretized with quadratic solid elements such as shown in Figure 6.4. A parametric study is carried out varying global size of those elements in order to reach a solution in both thermal and structural analyses which are independent to the element size and number. The size of elements takes special importance in thermal problems involving radiation, since the view factors calculations depend on it, an unoptimized mesh can lead to unprecise results in radiation problems. Figure 6.5 shows the resulting mesh.

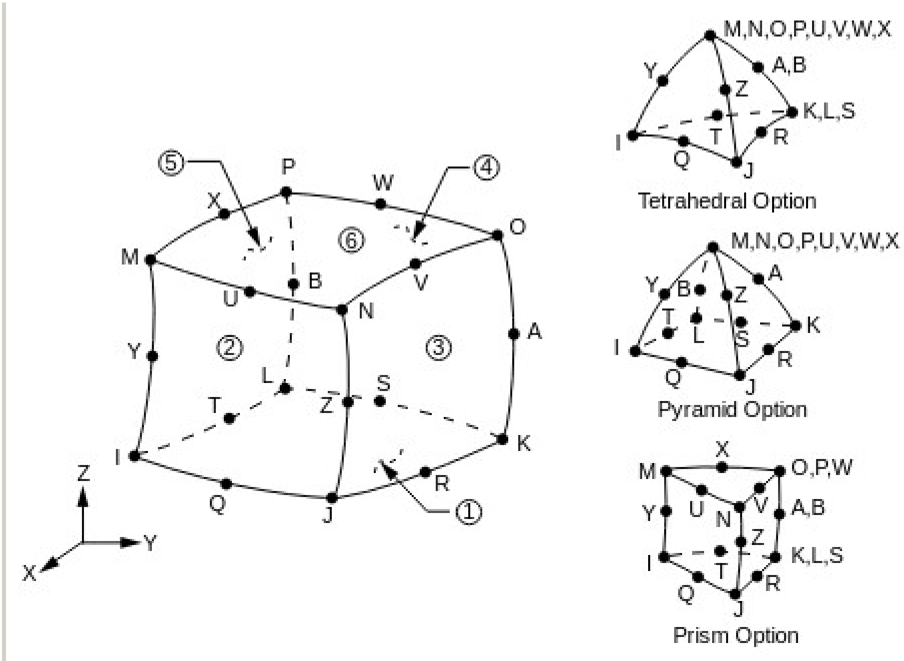

Figure 6.4 Quadratic solid element.

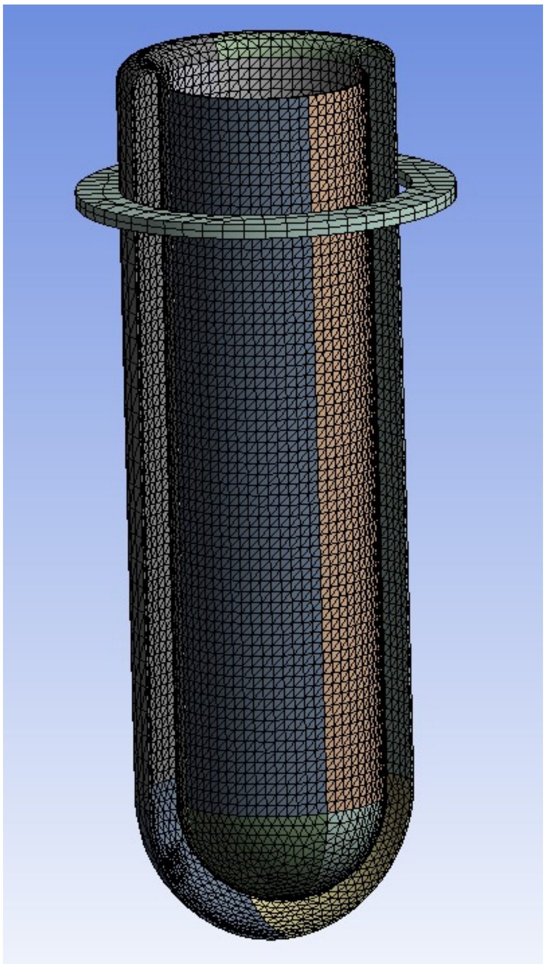

Figure 6.5. Model mesh.

6.1.3. Thermal model

Once the model has been meshed, the thermal analyses can be done. A series of assumptions and simplifications have been made, they well be explained bellow.

The thermal conditions within the reactor annulus will affect the behavior of the solar receiver studied in the present sub task, in other words, it is a coupled problem between the particle cloud conditions (composed by carbon dioxide and limestone particles) contained in the reactor annulus and the thermal conditions in the receiver cavity. An energy balance has to be done.

The ideal approach to solve the coupled problem explained above, would be to set a Conjugate Heat Transfer analysis (CHT), setting as an exchange boundary, the surface of the solar receiver at the reactor annulus side. On one hand, a CFD analysis is set to solve for the particle cloud problem, this analysis will have as one of its boundary conditions, the wall temperature at the exchange boundary. On the other hand, a thermal analysis of the solar cavity is set, and one of its boundary conditions would be the convective conditions at the exchange boundary, that is: near wall temperature and convection coefficient. Both analyses are carried out, passing information to each other until a convergence criterion is reached at the exchange boundary surface. All this process can be done automatically by using a single engineering software suite.

Since the CFD analysis of the particle cloud at the reactor annulus, and the thermal analysis of the solar receiver are being developed by different partners of the consortium, and each one of the analyses requires a long development, at the time of the writing this deliverable it was impossible to set the CHT problem. Therefore, to set the thermal analysis of the solar reactor, which is the scope of this deliverable, the ideally coupled problem is decoupled by making some assumptions and simplifications, which are explained below. The CHT analysis will have to be carried out as a next step in the project.

The focus of the solar calciner for VM matters will be set on the solar receiver solid (shown in orange in Figure 6.3), the surrounding shell (blue) will be used as an abstraction of the $CaCO_3$ and CO_2 particle cloud, so that it can be accounted for somehow. Two different configurations have been studied: with and without quartz window at the top of the receiver cavity.

6.1.4. Thermal Boundary Conditions

The following boundary conditions have been imposed to the thermal analysis model:

1. Solar Heat Flux: Heat flux coming from the secondary reflector obtained in Section 5 is mapped into the interior of the reactor cavity as depicted in Figure 6.6. The Total Solar Heat Flux imposed for each studied case is summarized in Table 6.1.
2. Radiation at the receiver cavity outer surface: an open enclosure has been set between all surfaces conforming the cavity interior and ambient, so that they can irradiate heat to each other, an emissivity value of 0.8 is used for all walls, the ambient temperature is set to 25 ºC. For both cases, with and without quartz window, the radiation exchange with ambient is the same.
3. Convection at the receiver cavity outer surface: the ambient temperature at which the solar receiver exchanges energy by convection, together with the convection film coefficient at its wall are imposed. In all cases of study, values of $h=2.5\ W/(m^2K)$ and $T_{bulk}=25ºC$ are used.
4. Convection at the cavity inner surface facing the reactor annulus: the $CaCO_3$ and CO_2 particle cloud bulk temperature (T_p) and the convection film coefficient are imposed at this surface, as stated before, this condition is ideally calculated by a CFD analysis. At this stage of the project they are obtained indirectly by simple energy balance calculations. Table 6.1. shows values for T_p for each studied case, while the film coefficient is $h=10\ W/(m^2K)$ for all walls in this boundary condition.
5. Radiation at the rector annulus: A radiation enclosure between all surfaces forming the reactor annulus is set. While the emissivity of the walls of the solar receiver were taken as the ones corresponding to the real material (0.8), the ones corresponding to the surrounding shell are set as the particle cloud ones (0.33).

6. Temperature at the outer surface of the shell: The temperature of the particle cloud is imposed. T_p in Table 6.1.

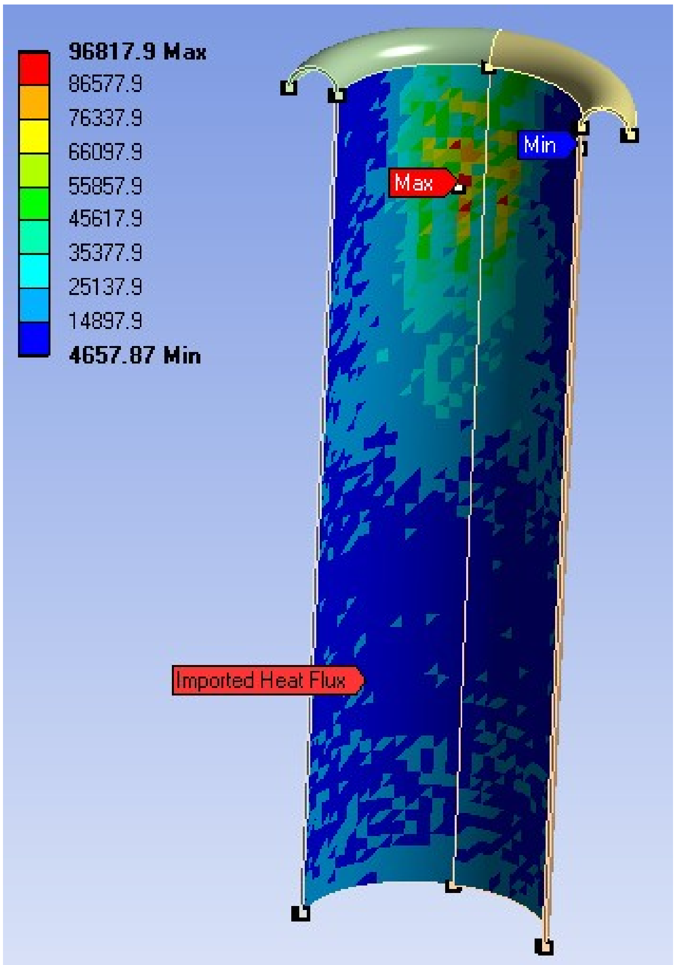

Figure 6.6. Solar Heat Flux boundary condition.

6.1.5. Thermal Model Results

Several models have been solved, varying their boundary conditions. Temperature field distributions directly depend mainly from the Solar Heat Flux applied, but also from the particle cloud inside the annulus that is assumed and the emissivity values specified at the radiation enclosures. Likewise, as stated before, the meshing also plays an important role, but in this case is just for precision matters. Thus, an optimization process has been carried out in order to get a convenient temperature field at the solar reactor cavity, that is, trying to get results for the temperature field distribution as even as possible to prevent spatial gradients that give rise to thermal stresses and below the maximum admissible temperature of the material, with a value of T_{max} = 1150ºC.

High temperature localized peaks are undesirable for two reasons: the heat flux provided to the reactor annulus will also be uneven which is not good for the calcination reaction, and high thermal stresses will be generated at those zones when the structural mechanic analysis is done. A short history of the evolution of the models and their results will be presented below, ending with the best optimized results obtained so far.

Two different models have been tested, namely:

1. R=0.552, with solar reflectivity of the receiver material equals 0.552, clean and smooth surface, without heat treatment and non-oxidized (see appendix)
2. R=0.81, with solar reflectivity of the receiver material equals 0.81, very high reflectivity to compare to normal values (0.552)

For each model, two variants are simulated

1. With Quartz window (w/), or
2. Without Quartz window (w/o)

For the model with quartz window (w/), the convection to ambient is neglected due to the action of the window that prevents the heated air plume to be released from the receiver cavity. Eventually, two different particles cloud temperature have also been used:

1. T_p=900ºC, the minimum temperature at which the calcination can occurs, the turning temperature of CaCO3/CO2
2. T_p=985ºC, the temperature where the calcination takes place completely

We first show the thermal model results and afterwards in Section 6.1.6 the mechanical results.

Model R=0.81 Without Window. Tp=900 ºC

1. Temperature Field

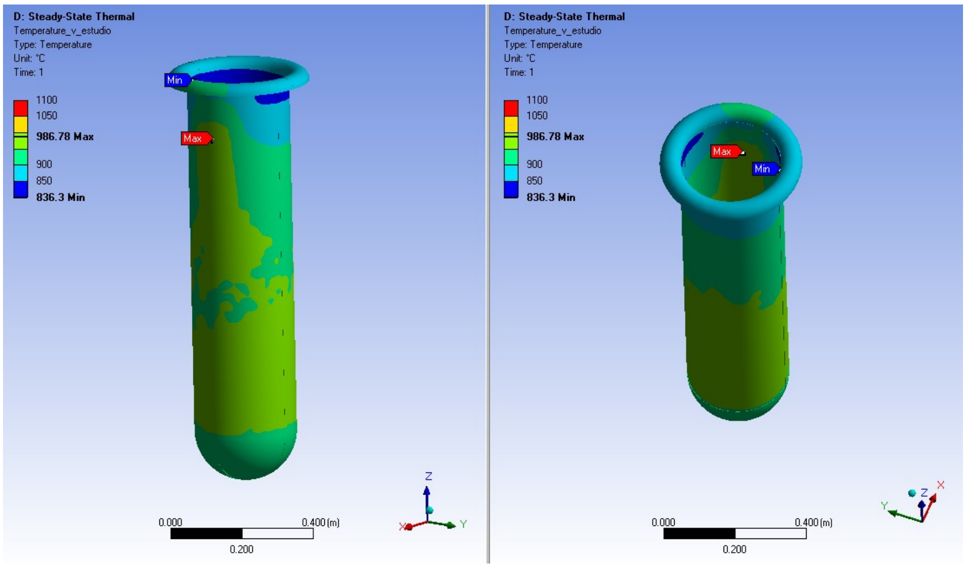

Figure 6.7. Temperature field at the solar cavity.

2. Heat Flux Distribution going to reaction annulus

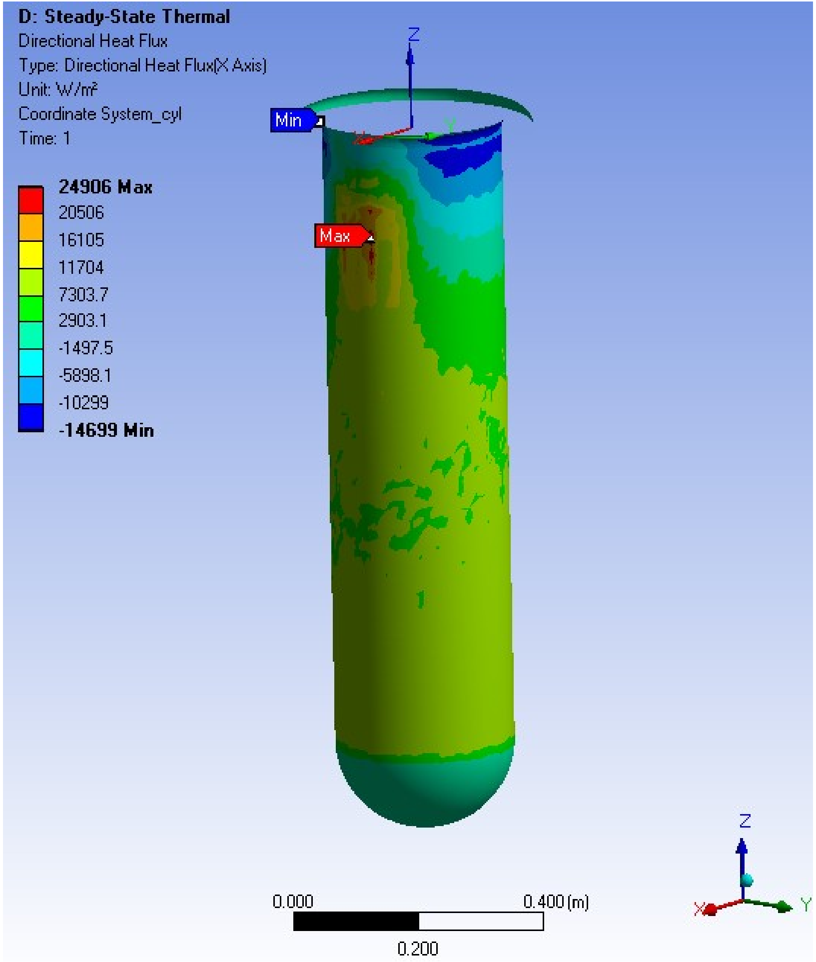

Figure 6.8. Heat Flux distribution going to reactor annulus.

Model R=0.81 Without Window. Tp=985 ºC

1. Temperature Field

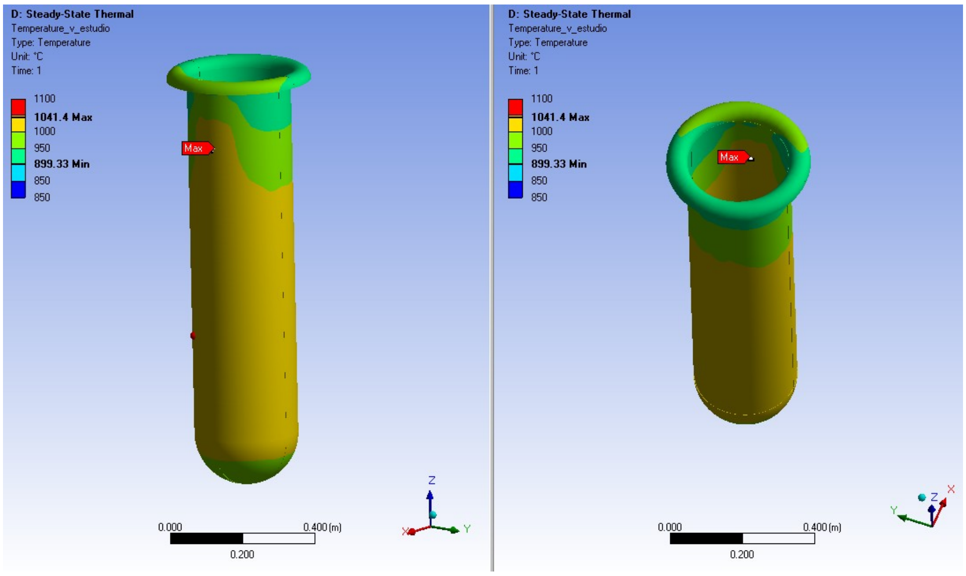

Figure 6.9. Temperature field at the solar cavity.

2. Heat Flux Distribution going to reaction annulus

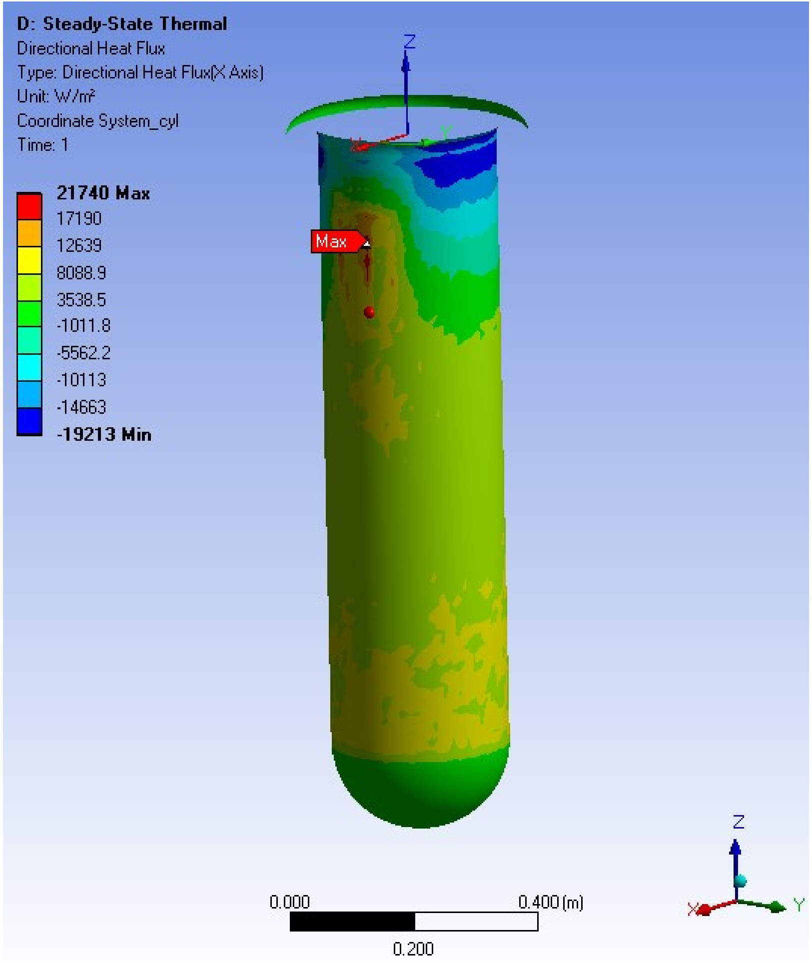

Figure 6.10. Heat Flux distribution going to reactor annulus.

Model R=0.552 Without Window. Tp=900 ºC

1. Temperature Field

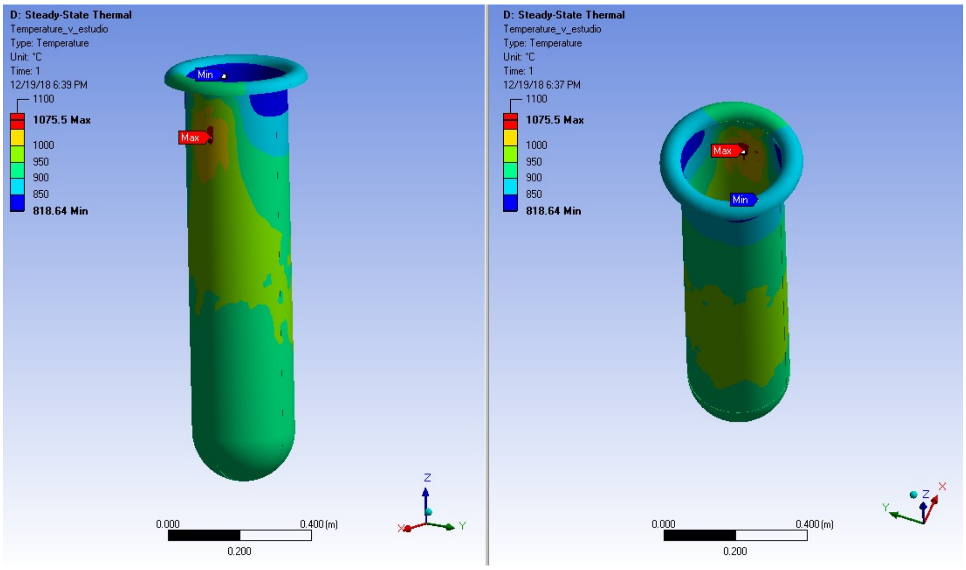

Figure 6.11. Temperature field at the solar cavity.

2. Heat Flux Distribution going to reaction annulus

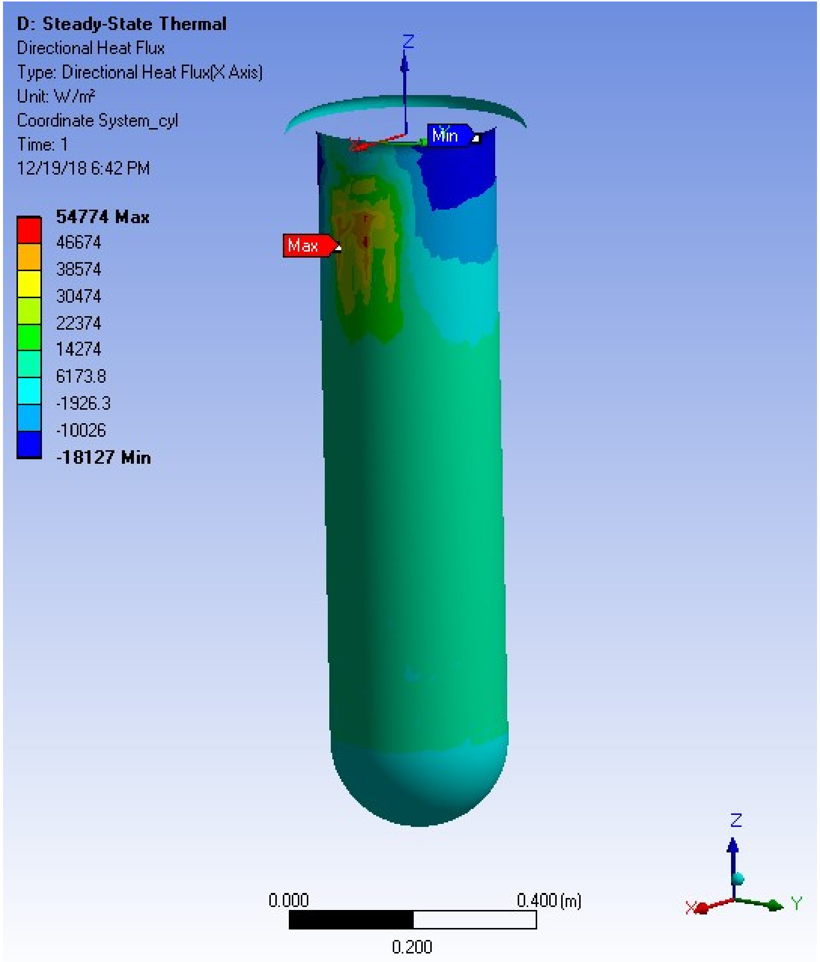

Figure 6.12. Heat Flux distribution going to reactor annulus.

Model R=0.552 Without Window. Tp=985 ºC

1. Temperature Field

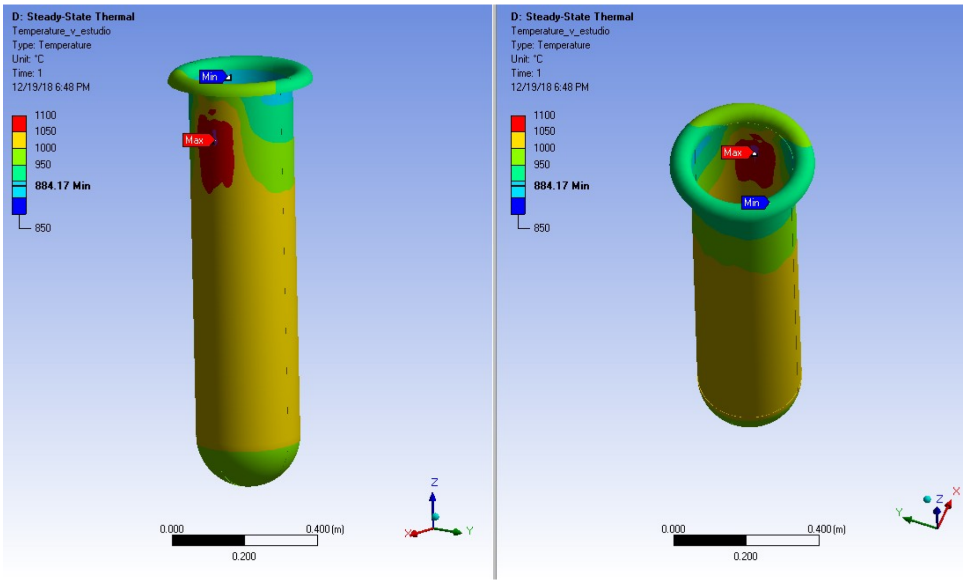

Figure 6.13. Temperature field at the solar cavity.

2. Heat Flux Distribution going to reaction annulus

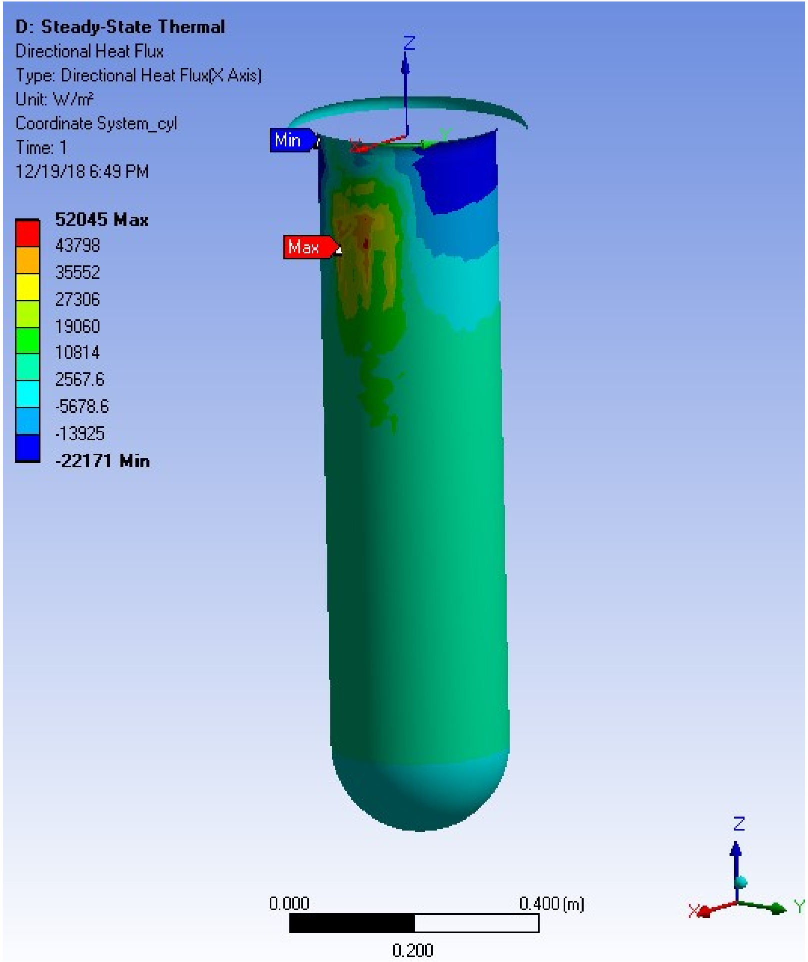

Figure 6.14. Heat Flux distribution going to reactor annulus.

Model R=0.81 With Window. Tp=900 ºC

1. Temperature Field

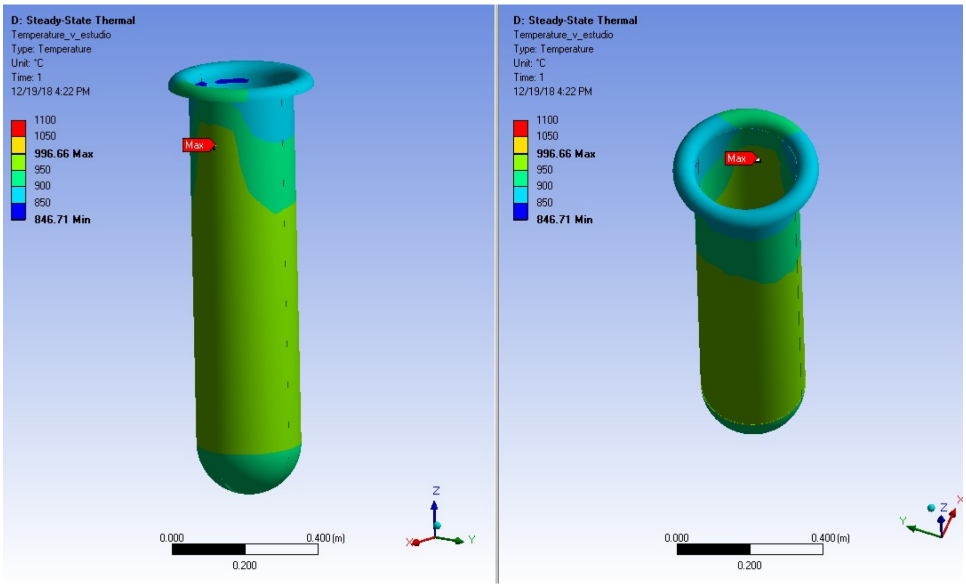

Figure 6.15. Temperature field at the solar cavity.

2. Heat Flux Distribution going to reaction annulus

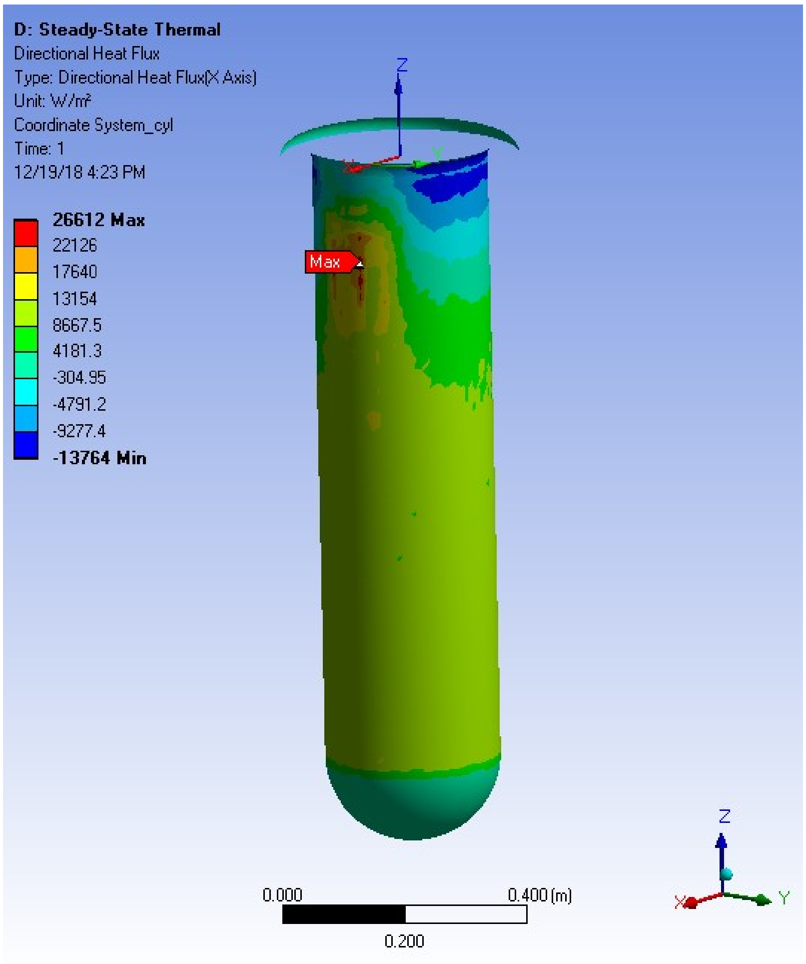

Figure 6.16. Heat Flux distribution going to reactor annulus.

Model R=0.81 With Window. Tp=985 ºC

1. Temperature Field

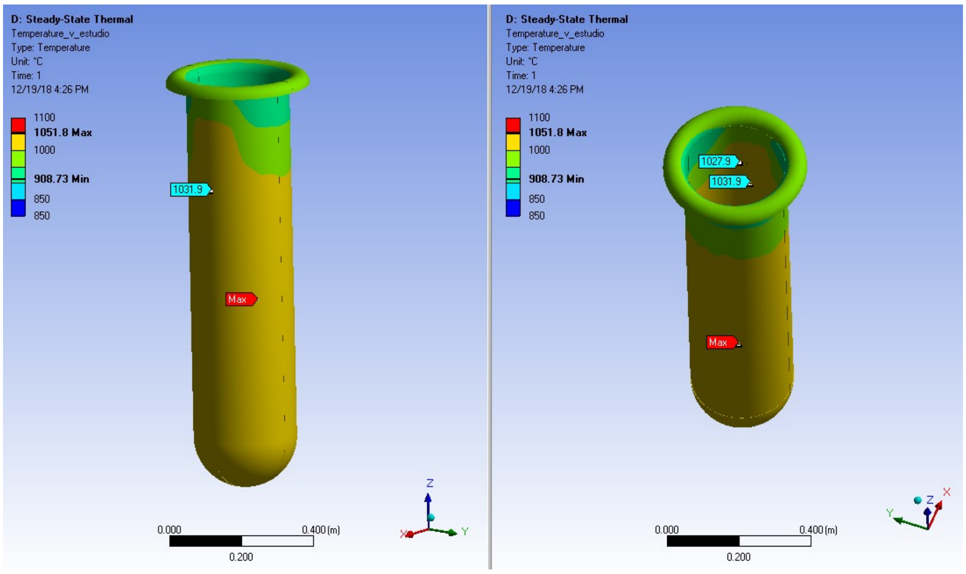

Figure 6.17. Temperature field at the solar cavity.

2. Heat Flux Distribution going to reaction annulus

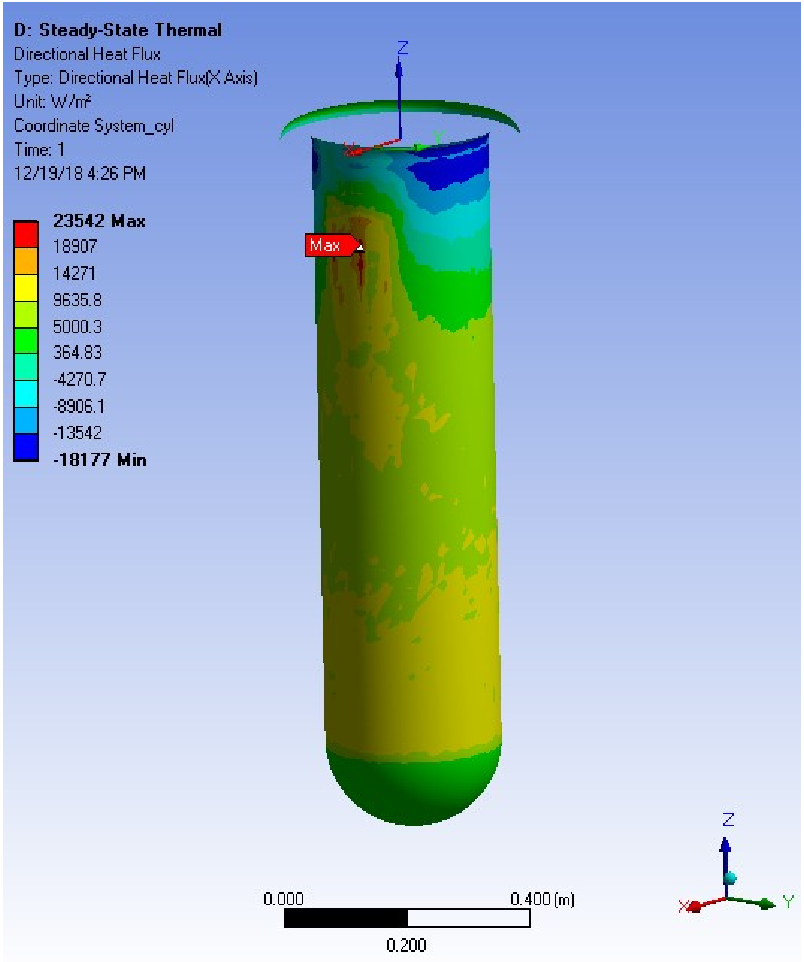

Figure 6.18. Heat Flux distribution going to reactor annulus.

Model R=0.552 With Window. Tp=900 ºC

1. Temperature Field

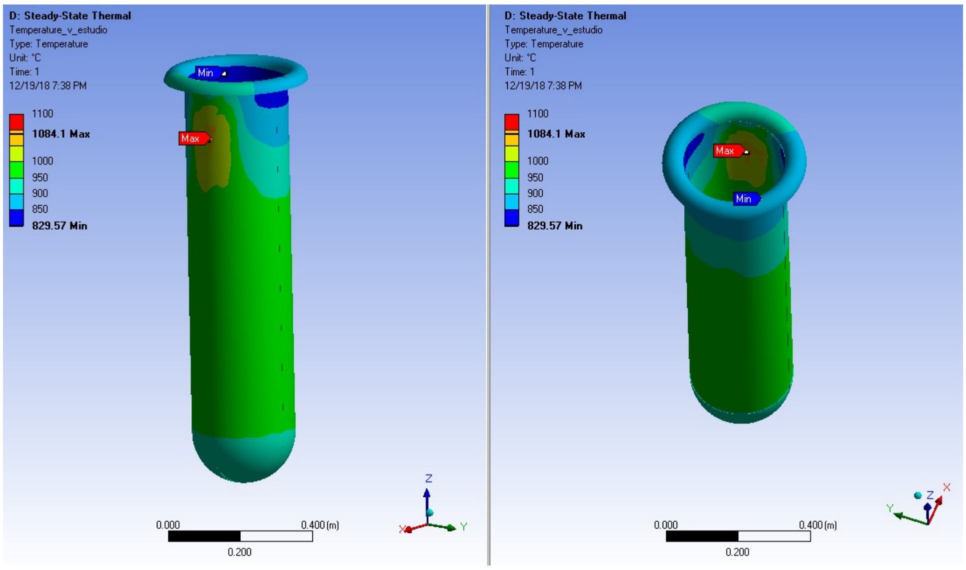

Figure 6.19. Temperature field at the solar cavity.

2. Heat Flux Distribution going to reaction annulus

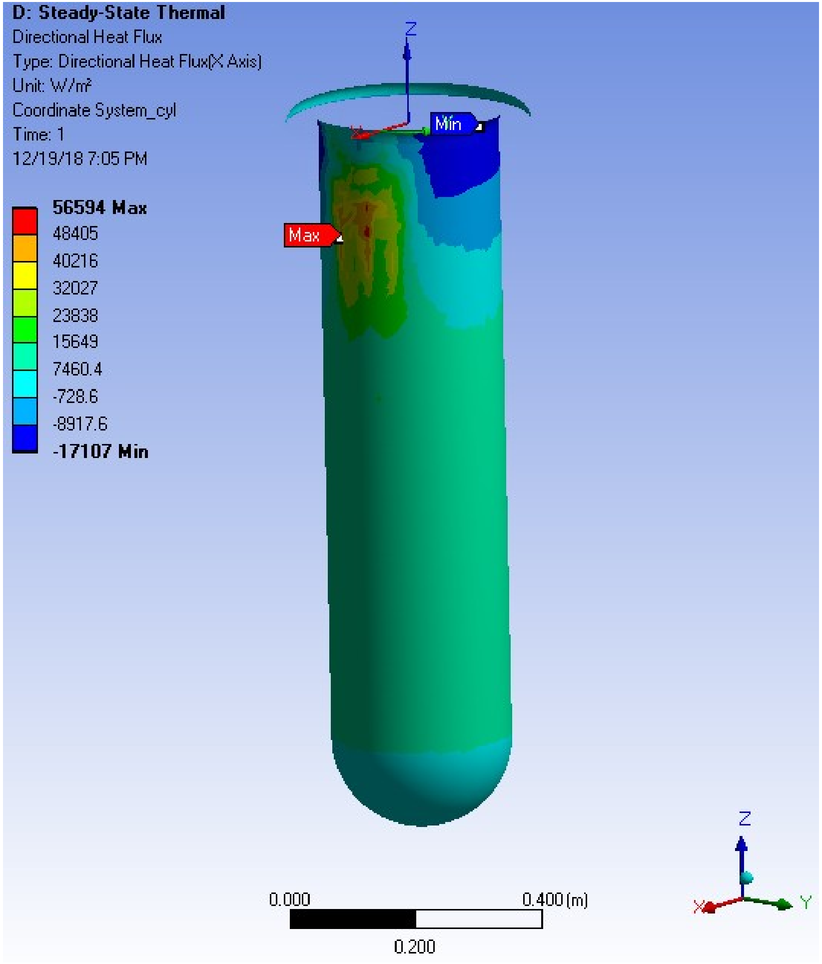

Figure 6.20. Heat Flux distribution going to reactor annulus.

Model R=0.552 With Window. Tp=985 ºC

1. Temperature Field

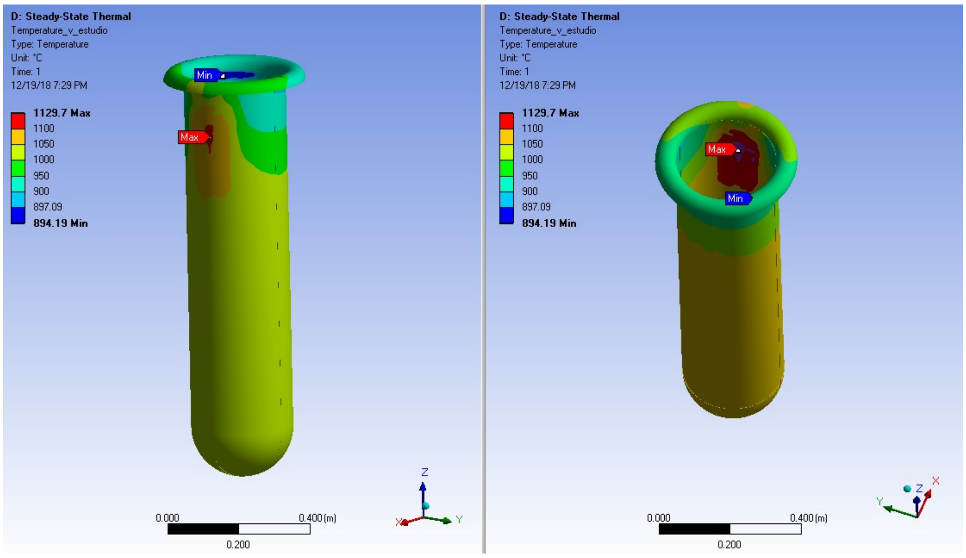

Figure 6.21. Temperature field at the solar cavity.

2. Heat Flux Distribution going to reaction annulus

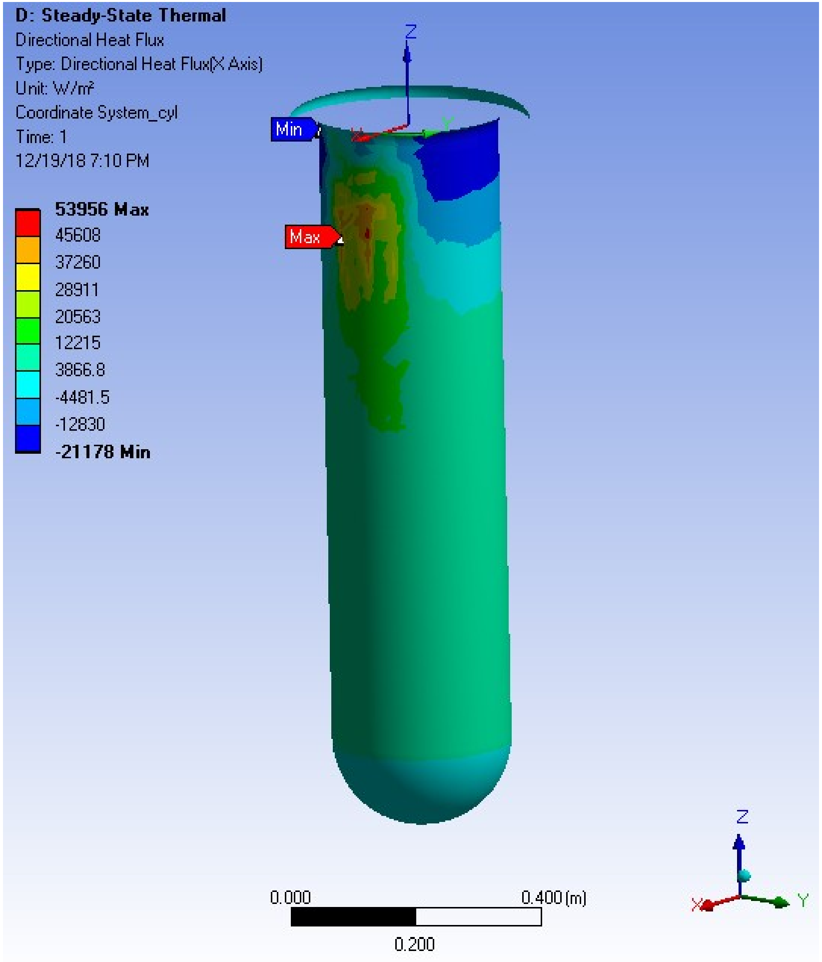

Figure 6.22. Heat Flux distribution going to reactor annulus.

6.1.6. Structural Model Results

For the mechanical problem at hand, the temperature field from the thermal calculation is imposed on the solid domain and mechanical boundary conditions are applied, namely:

1. Frictionless support at the base of the half-torus-like shape top part that connects with the shell. This is to restrict the vertical movement of the part, allowing this face to move only in the Z plane where it is contained. See Figure 6.23.
2. All displacement degrees of freedom at a node contained at a quadrant of the previous surface 1), to prevent the part from moving freely within the Z plane where the face is located. At this moment the solid can still rotate in the Z plane around the selected node. See Figure 6.24.
3. Displacement in the X direction at a node located at the same surface in 1), and in the next quadrant to 2). This will complete the requirements to prevent rigid solid motions. See Figure 6.25.

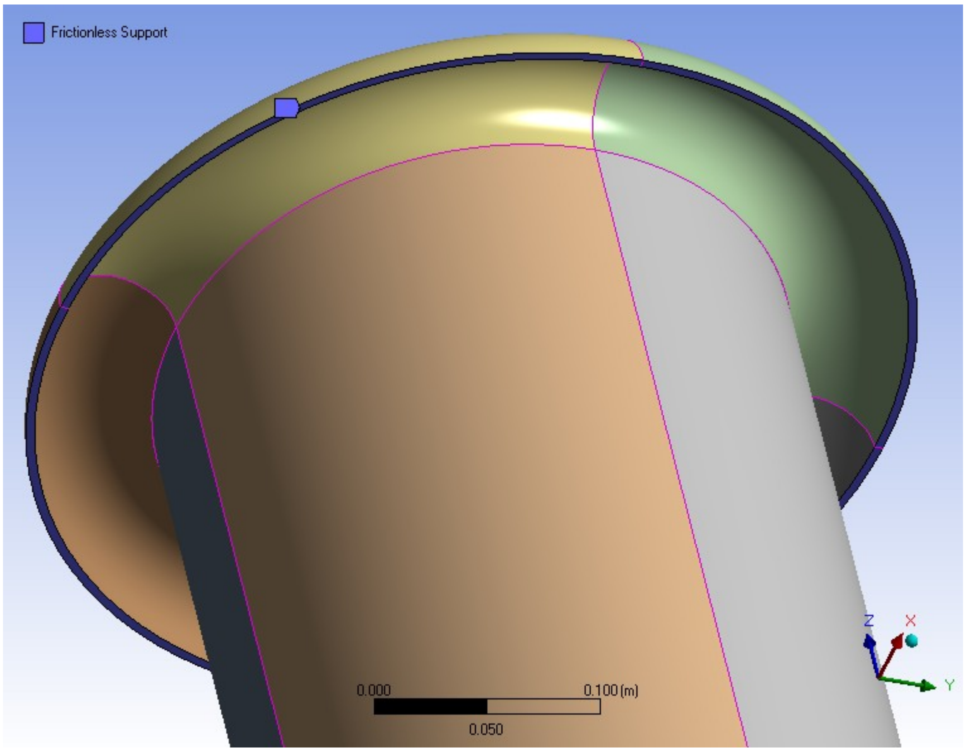

Figure 6.23. Frictionless boundary condition at surface.

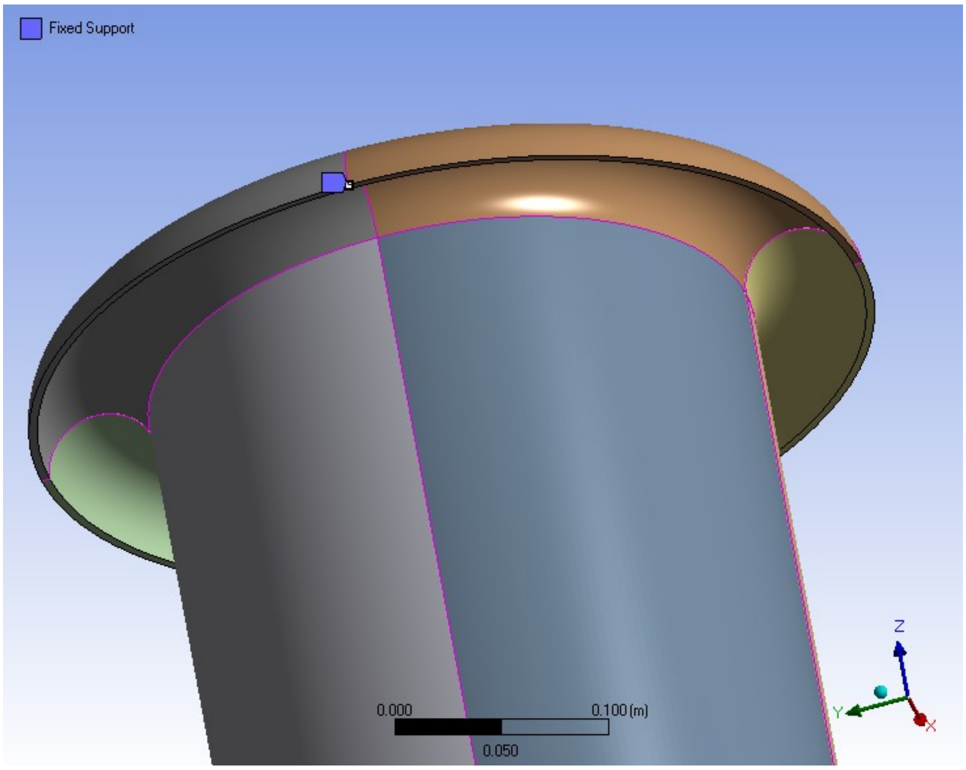

Figure 6.24. Fixed support boundary condition at node.

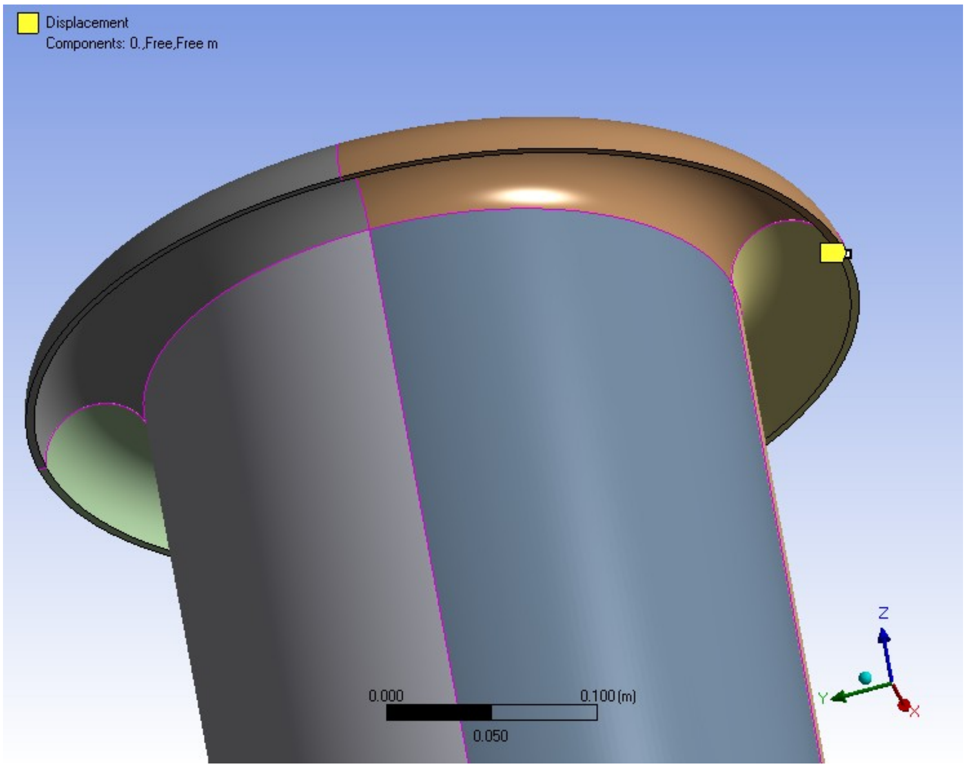

Figure 6.25. Displacement in the X direction=0 boundary condition at node.

The previous boundary conditions allow the base of the curved top part to expand itself due to temperature, while preventing the rigid body motion. This will allow to focus the attention on the mechanical behavior on the most critical part of the solar receiver: The tube or cylinder part.

To compare the different models, Von Mises stress is monitored on the radiation heating surface of the receiver cavity.

Model R=0.81 Without Window. Tp=900 ºC

1. Von Mises Stresses

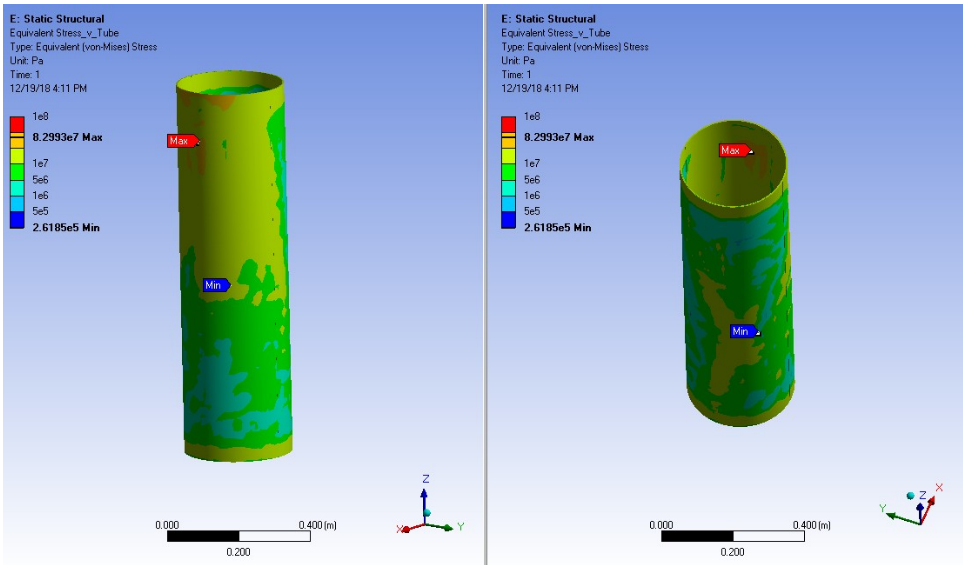

Figure 6.26. Von Mises Equivalent Stress at the solar cavity tube.

Model R=0.81 Without Window. Tp=985 ºC

1. Von Mises Stresses

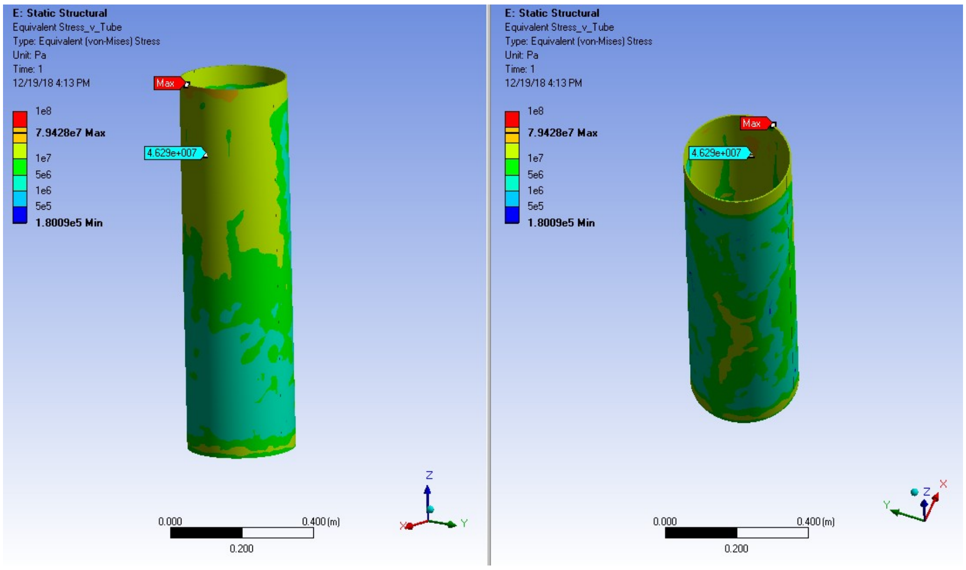

Figure 6.27. Von Mises Equivalent Stress at the solar cavity tube.

Model R=0.552 Without Window. Tp=900 ºC

1. Von Mises Stresses

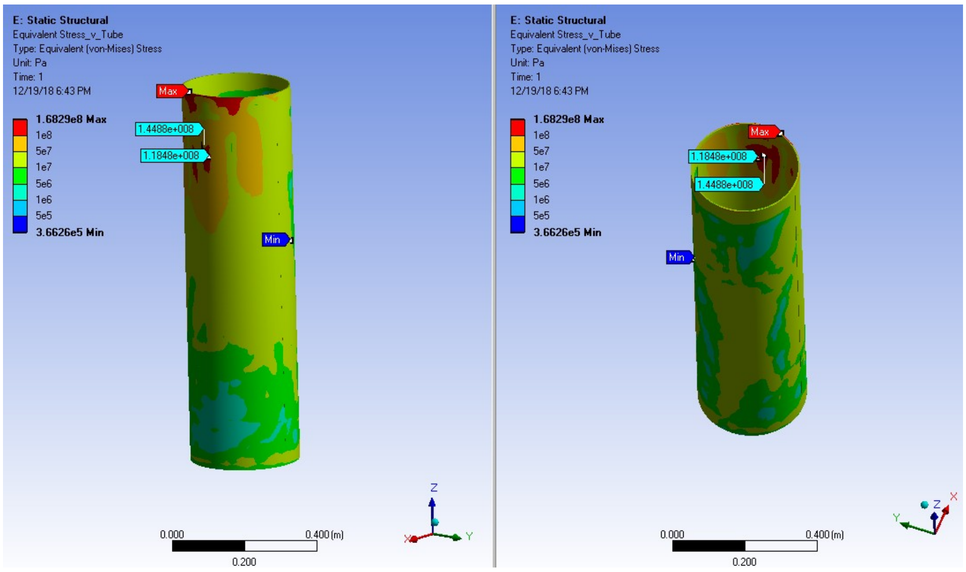

E: Static Structural
Equivalent Stress_v_Tube
Type: Equivalent (von-Mises) Stress
Unit: Pa
Time: 1
12/19/18 6:43 PM

E: Static Structural
Equivalent Stress_v_Tube
Type: Equivalent (von-Mises) Stress
Unit: Pa
Time: 1
12/19/18 6:43 PM

Figure 6.28. Von Mises Equivalent Stress at the solar cavity tube.

Model R=0.552 Without Window. Tp=985 ºC

1. Von Mises Stresses

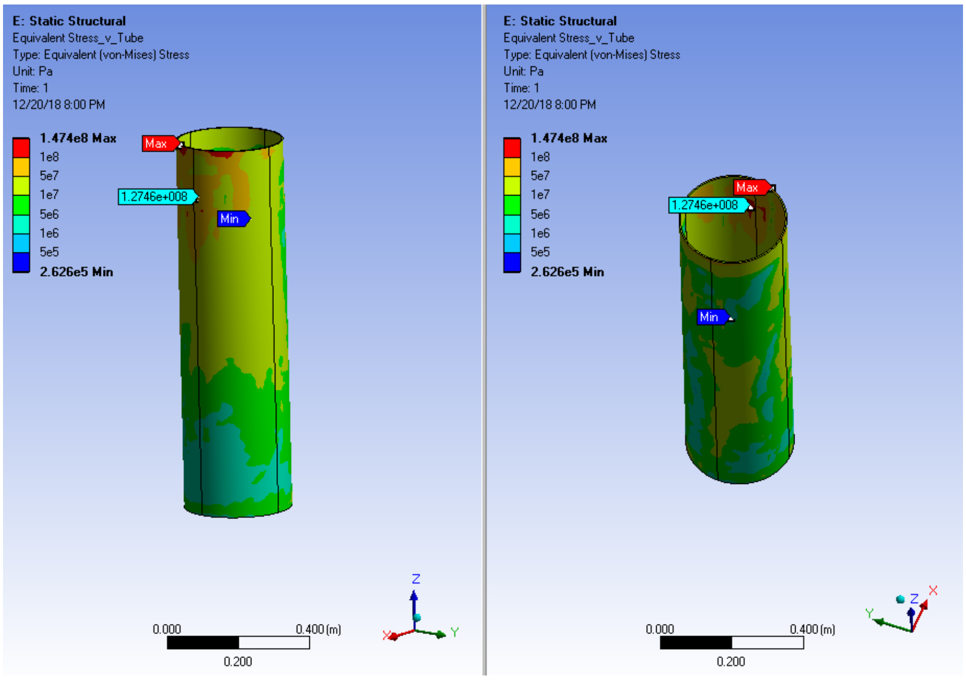

E: Static Structural
Equivalent Stress_v_Tube
Type: Equivalent (von-Mises) Stress
Unit: Pa
Time: 1
12/20/18 8:00 PM

E: Static Structural
Equivalent Stress_v_Tube
Type: Equivalent (von-Mises) Stress
Unit: Pa
Time: 1
12/20/18 8:00 PM

Figure 6.29. Von Mises Equivalent Stress at the solar cavity tube.

Model R=0.81 With Window. Tp=900 ºC

1. Von Mises Stresses

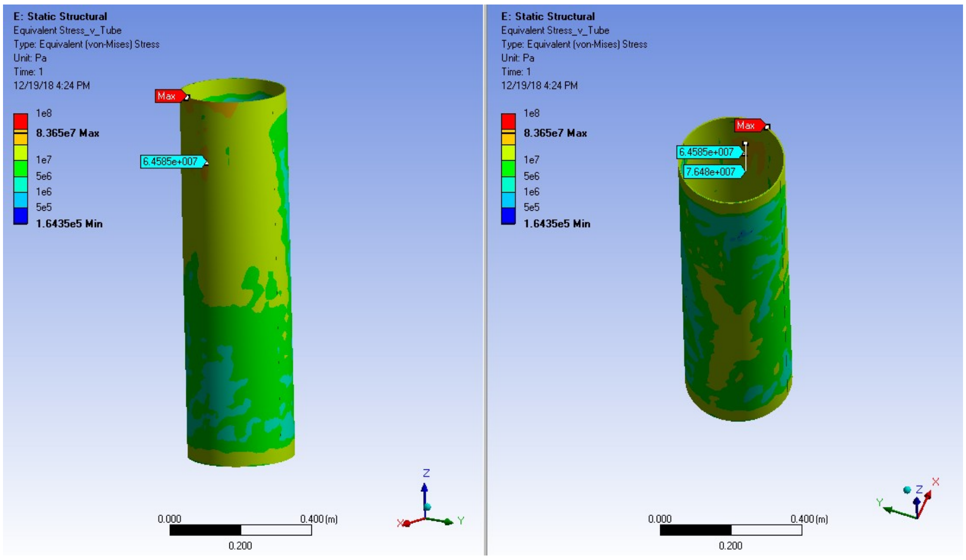

Figure 6.30. Von Mises Equivalent Stress at the solar cavity tube.

Model R=0.81 With Window. Tp=985 ºC

1. Von Mises Stresses

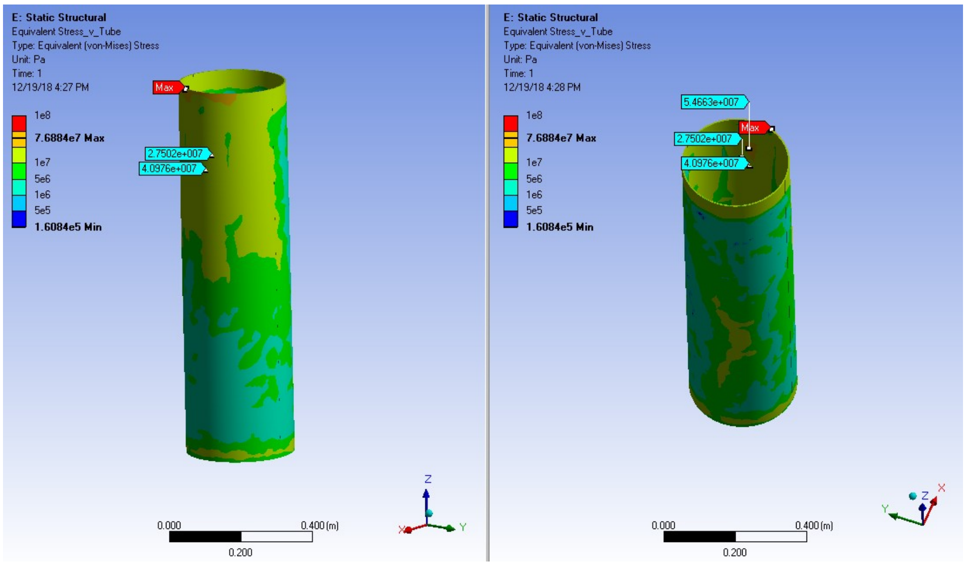

Figure 6.31. Von Mises Equivalent Stress at the solar cavity tube.

Model R=0.552 With Window. Tp=900 ºC

1. Von Mises Stresses

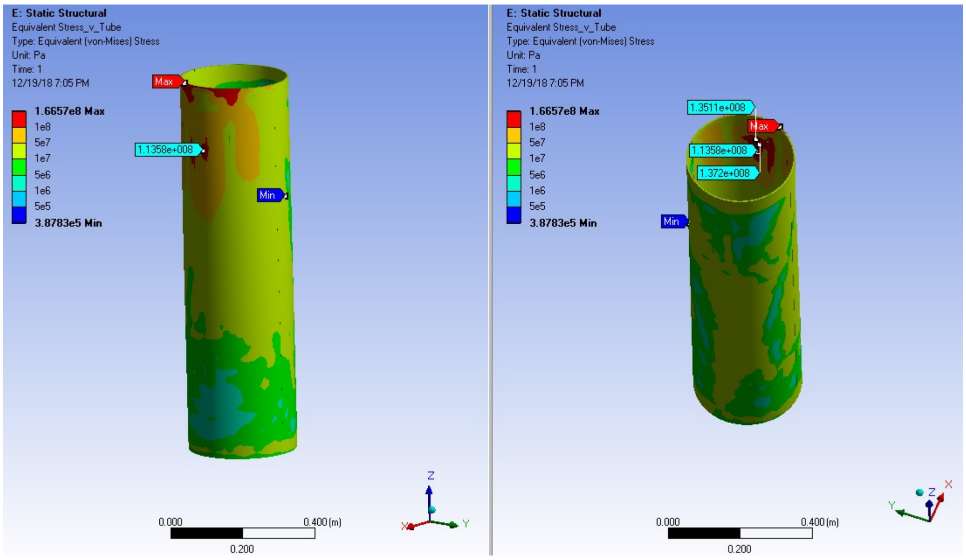

E: Static Structural
Equivalent Stress_v_Tube
Type: Equivalent (von-Mises) Stress
Unit: Pa
Time: 1
12/19/18 7:05 PM

E: Static Structural
Equivalent Stress_v_Tube
Type: Equivalent (von-Mises) Stress
Unit: Pa
Time: 1
12/19/18 7:05 PM

Figure 6.32. Von Mises Equivalent Stress at the solar cavity tube.

Model R=0.552 With Window. Tp=985 ºC

1. Von Mises Stresses

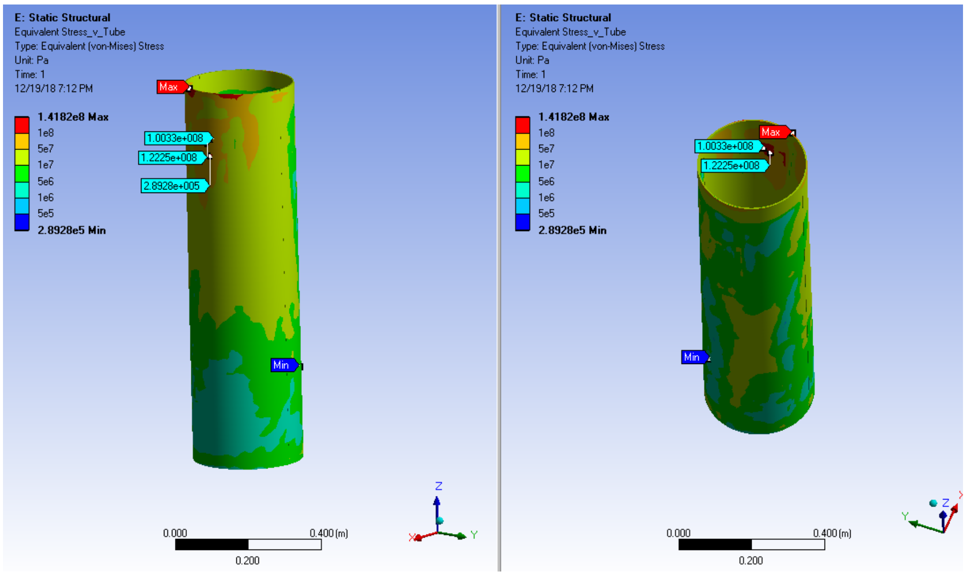

E: Static Structural
Equivalent Stress_v_Tube
Type: Equivalent (von-Mises) Stress
Unit: Pa
Time: 1
12/19/18 7:12 PM

E: Static Structural
Equivalent Stress_v_Tube
Type: Equivalent (von-Mises) Stress
Unit: Pa
Time: 1
12/19/18 7:12 PM

Figure 6.33. Von Mises Equivalent Stress at the solar cavity tube.

6.1.7. Results discussion

The thermal model acts as a simple system with one input (solar radiation) and two outputs (heat loses and heat transferred to the particles cloud), see Figure 6.34. The input is the absorbed radiation of the receiver cavity outer wall coming from the solar field and secondary reflector, Q_{in} [W/m^2]. This, as explained in Section 5, strongly depends on the surface solar reflectivity (or its dual, the solar absorptivity) and of course on the nature and quality of the radiation coming from the secondary reflector. The first (undesirable) output are the thermal loses of the cavity, mainly radiation and convection (w/o quartz window) to ambient, Q_{loss} [W]. Eventually, the second output is the heat or energy transferred to the particle cloud reaction, Q_p [W]. Both outputs strongly depend on the particle cloud temperature T_p. On the one hand, radiation loses are proportional to the receiver wall temperature T_w to the fourth, which depends on the applied heat flux coming from the solar radiation Q_{in}, and the temperature at which it radiates on the annulus which is no other than T_p. It also depends linearly on T_w via convection loses. Therefore $Q_{loss} = f(T_w=f(T_p))$. On the other hand, the energy transferred to the particle cloud Q_p depends on $(T_w-T_p)^4$ for radiation exchange and on (T_w-T_p) on convective transfer. If T_p is high, of the order of 900ºC, thermal radiative exchange is predominant. For that, T_w must be higher than T_p if energy is to be transferred to the particle cloud. Hence, radiation loses to ambient are very high. In this configuration and temperature range, radiation losses to ambient are going to be very high, almost regardless of the shape of the cavity and its view factor to ambient.

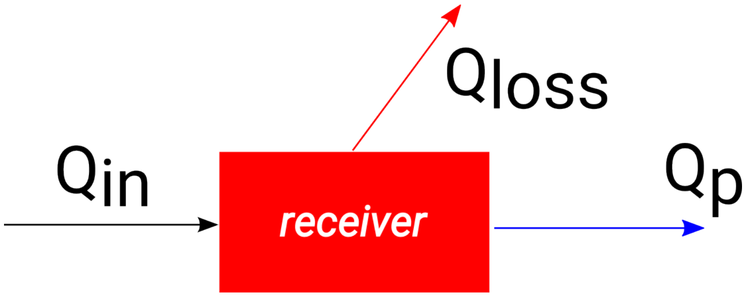

Figure 6.34. Heat distribution in the cavity receiver to reactor.

As shown in Table 6.1, the following conclusions can be extracted from the thermal analysis:

- Radiation loses to ambient are of the order of 50% of the inlet energy. At the present temperature range, this is almost impossible to improve
- Convection loses are of the order of 15% of the inlet energy but can be obviously neglected if the quartz window is used
- When T_p is higher, the thermal efficiency of the receiver cavity decreases due to higher loses, mainly radiative
- The maximum temperature at the receiver cavity wall, T_w, obviously increases with increasing T_p
- The maximum temperature at the receiver cavity wall, T_w, decreases when reflectivity of the receiver cavity material is increased. This, as explained in Section 5, is due to the better flux distribution, more homogeneous, generated by reflections inside the cavity. When this happens, heat flux peaks are lower and so it's the resulting wall temperature
- In most cases, T_w^{MAX} is lower than the material maximum allowable temperature which lies around 1150 ºC. Improving the flux distribution via better material reflectivity and better solar tracing, this temperature can be further decreased but the saturation of this decrease is governed by the value of T_p

For the mechanical problem at hand, the following conclusions can be extracted:

- When T_p is higher, although T_w is also higher, the temperature gradient is lower and stress is lower too, almost 25%
- For higher reflectivity, the temperature distribution is more homogeneous, the spatial gradients are lower and stress peaks are lower, almost a 42%
- The presence of the quartz window has a slight effect on the stress, lowering its value around 5%

- In all cases stress seems too high for the temperatures reached at the metal and it is recommended to take some actions in order to reduce it.
- Although for temperatures higher than 600ºC, the datasheet of the material recommends to compare to the creep rupture strength, as the system is prototype, it will not be exposed to these very high thermal loads for too long, only hours not thousands of hours, creep shouldn't be a problem for the pilot plant. For the real scale system, this could be an issue

For reference and detailed field variables, see Figures above.

Table 6.1.-Indirect CFC Solar Calciner Results Summary.

MODELO	**T_P [ºC]**	**T_W^{MAX}[ºC]**	**Total Solar HF [W]**	**Total HF to Reactor [W]**	**Efficiency [%]**		**Maximum VM Stress at solar flux peak [MPa]**
Modelo R=0.81 w/o window.	900	986.78	14027	5734.47	0.41		83
Modelo R=0.81 w/o window.	985	1141.4	14027	4057.22	0.29		62
Modelo R=0.552 w/o window.	900	1075.5	13728	5428.91	0.40		145
Modelo R=0.552 w/o window.	985	1121.5	13728	3762.53	0.27		127
Modelo R=0.81 w/ window.	900	996.66	14027	7774.68	0.55		80
Modelo R=0.81 w/ window.	985	1151.8	14027	6212.45	0.44		60
Modelo R=0.552 w/ window.	900	1084.1	14027	7449.43	0.54		137
Modelo R=0.552 w/ window.	985	1029.7	14027	5922.01	0.43		122

6.2. Indirect Cavity SiC Solar Calciner

6.2.1. Geometry Model

The solar receiver's cavity geometry configuration for the Indirect Cavity SiC Solar Calciner is inspired by previous projects carried out by VM. Figure 6.35 depicts a cross section of the solar cavity, based on a truncated pyramid. All dimensions are controlled parametrically.

The configuration is based on layering with different materials the solar receiver, where each material has its purpose. The aim of this design is to minimize heat flux trough the side walls, so that most of the solar power is directed to the bottom plate which will transfer the heat to the calciner area where the limestone circulates in a conveyor.

This prototype has direct opening to the exterior with no quartz window, which could be included in the future. A brief description of the layers will be presented below.

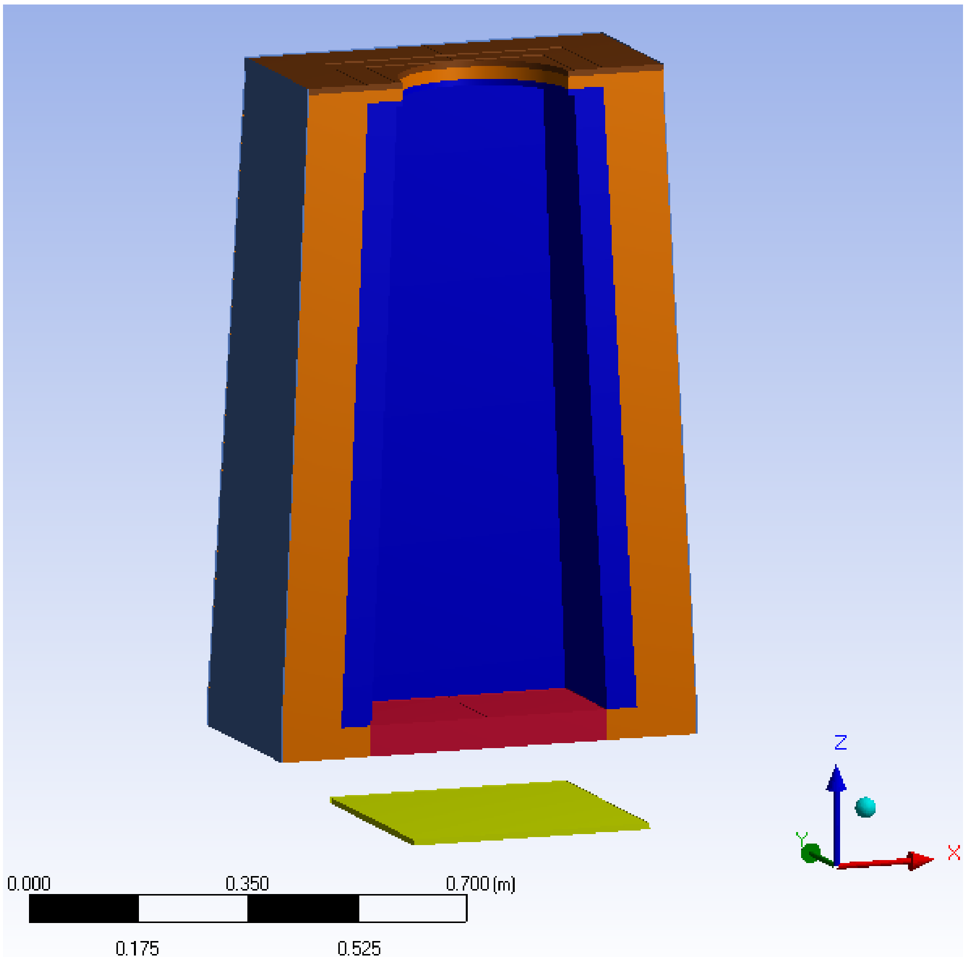

Figure 6.35. Indirect Cavity SiC Solar Calciner Receiver. Cross section.

Layer 1:

Colored in blue, it surrounds the interior side walls and around the top aperture. It is made of Scuttherm LT HW (see appendix C, side walls for the datasheet).

The main characteristic of this material is high reflexivity and low absorptivity, able to withstand very high temperatures. On the downside, it has a relatively high thermal conductance and that is why it has to be surrounded by layer 2.

Thickness is 50 mm for the lateral walls, and 10 mm for the top.

Layer 2:

Colored in orange, surrounds all Layer1 external walls. It is made of Microtherm-1000-RV1.

The main characteristic of this material is a very low thermal conductivity.

Thicknesses are 100 mm for the lateral walls, 50 mm for the bottom and 20 mm for the top.

Layer 3:

Colored in gray, it surrounds Layer 2 only at lateral walls. It's made out of AISI-304 steel.

The mission of this outer layer is to provide a mechanical frame to support all layers.

Thickness is 2mm.

Besides these three layers, an additional 10mm thick layer of Scuttherm (colored in brown) is added to the top of the receiver surrounding the aperture, just to reflect the spilled rays away from the receiver.

SiC plate:

Colored in red, it has rectangular shape that can be forced to be squared by the parametric modeling. It's made out of Silicon carbide (see datasheet properties in Annex D).

The mission of this plate is to collect the solar power and to transfer the heat flux to the underlying limestone particles for the calcination process.

The thickness of this plate is 50 mm.

The limestone particles are represented in the models by the green colored plate below the cavity.

The internal dimensions of the solar cavity are:

- 400x400 mm base.
- 300x300 mm top.
- 139.58 mm window radius.
- 1090 mm high.

6.2.2. Meshing

Exactly the same procedure described in Section 6.1.2 for the Indirect CFC Solar Calciner is followed for this prototype. Figure 6.8 shows the resulting mesh.

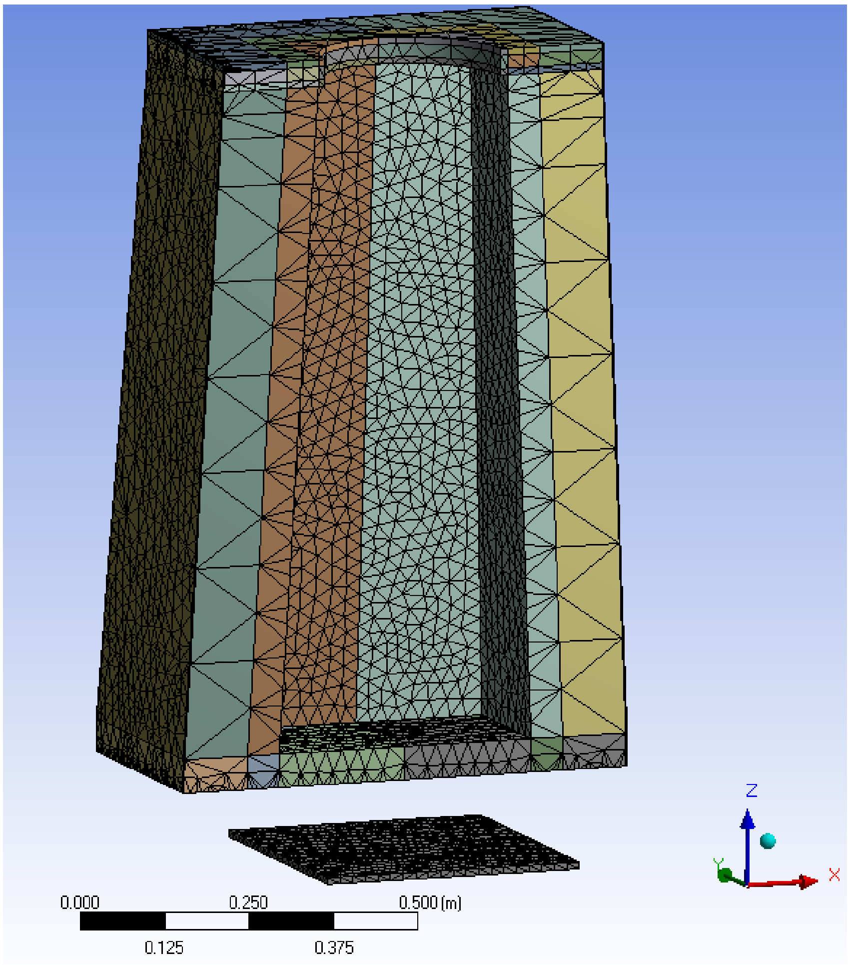

Figure 6.36. Indirect Cavity SiC Solar Calciner. Mesh.

6.2.3. Thermal Model

The current prototype is based on the concept that a conveyor transports the limestone and the solar receiver directs the heat flux vertically to it, minimizing the losses through the side walls.

6.2.4. Thermal Boundary Conditions

The following boundary conditions have been imposed to the thermal analysis model:

1. Solar heat flux: heat flux coming from the secondary reflector obtained in Section 5 is mapped into the interior of the receiver cavity as depicted in Figure 6.37.
2. Radiation at the cavity interior: an open enclosure has been set with all the surfaces conforming the cavity interior, so that they can irradiate heat to each other. Emissivity of all walls are provided (0.95 for the Scuttherm, and 0.9 for the SiC materials). The ambient temperature is set to 25 ºC.
7. Convection inside the cavity: the convection film coefficient at the walls is imposed, h=2.5 W/(m^{2}K) which corresponds to a temperature of 25ºC.
8. Convection at the cavity outer surfaces: the ambient temperature at the exterior of the solar receiver, together with the convection film coefficient at its wall are imposed. Values of T_{bulk}=25ºC and h=4.0 W/(m^{2}K) are used.
3. Radiation between the solar cavity bottom and the limestone plate: an open enclosure is defined between the two facing surfaces. The ambient temperature is set to 900ºC, while the emissivity of the SiC plate is 0.9 and the limestone plate is 0.95.

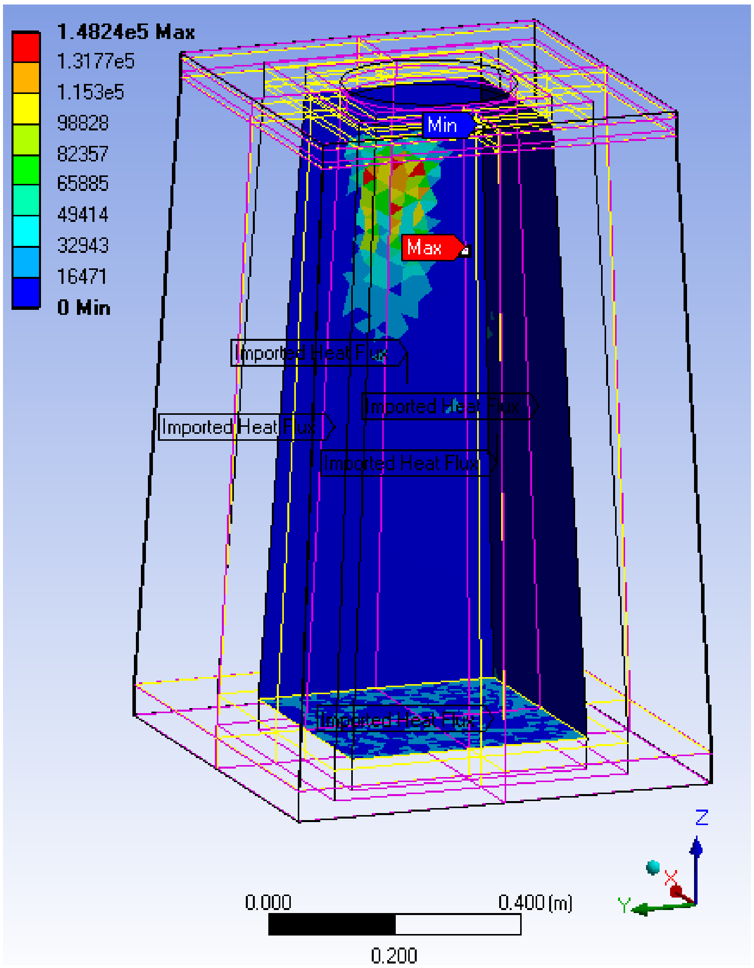

Figure 6.37. Solar Heat Flux boundary condition.

6.2.5. Thermal Model Results

Once the boundary conditions are applied, the model is ready to be solved. Two variants are simulated:

1. With Quartz window (w/), or
2. Without Quartz window (w/o)

Figure 6.38 depicts the global temperatures of a whole cavity section for both variants simulated.

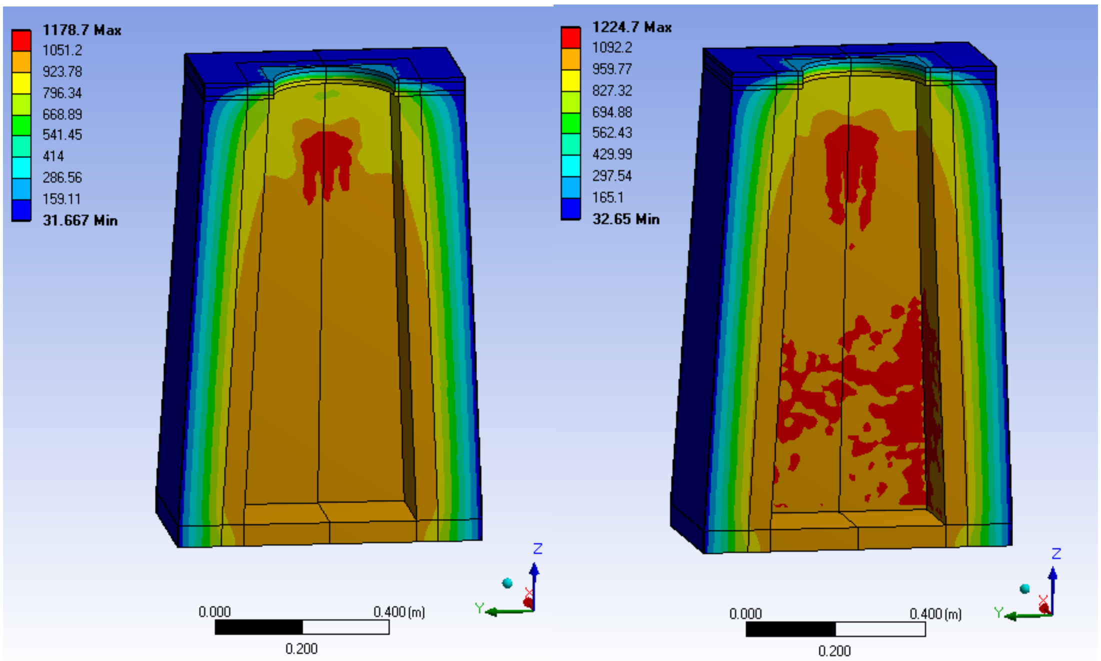

Figure 6.38. Temperature field in the whole cavity. W/o and W/ Window.

Next, it will be shown the temperature fields for each different material forming the cavity.

Figure 6.39 shows the temperature field at Layer 1, in which the solar radiation is applied, as expected the maximum global temperature is located in this body. Figure 6.40 depicts the temperature field at Layer 2. The temperature field for Layer 3 which is shown in Figure 6.41.

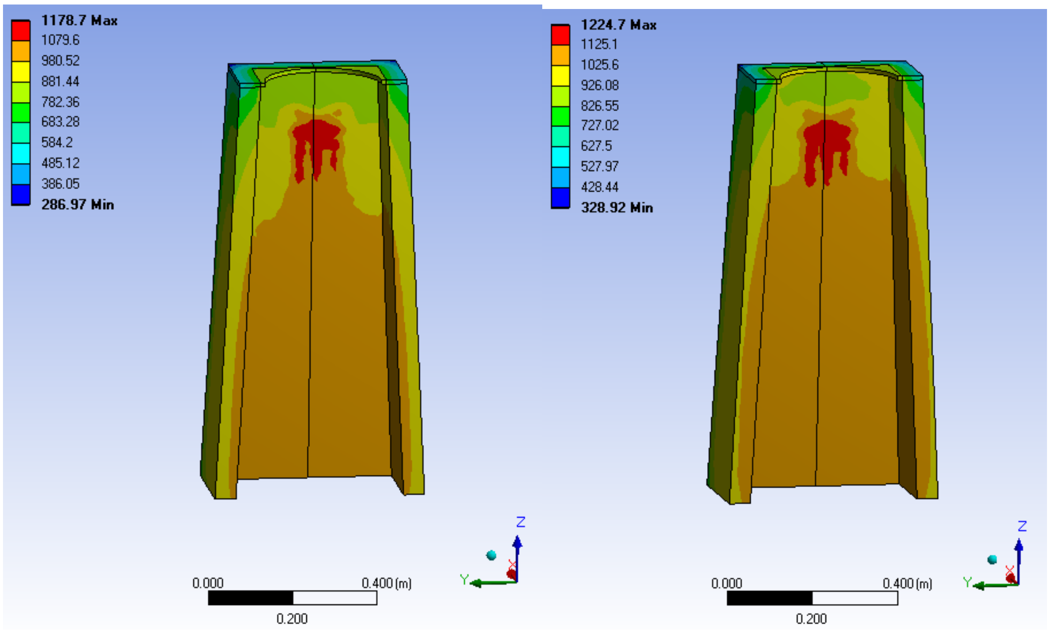

Figure 6.39. Temperature Field at Layer1. W/o and W/ Window.

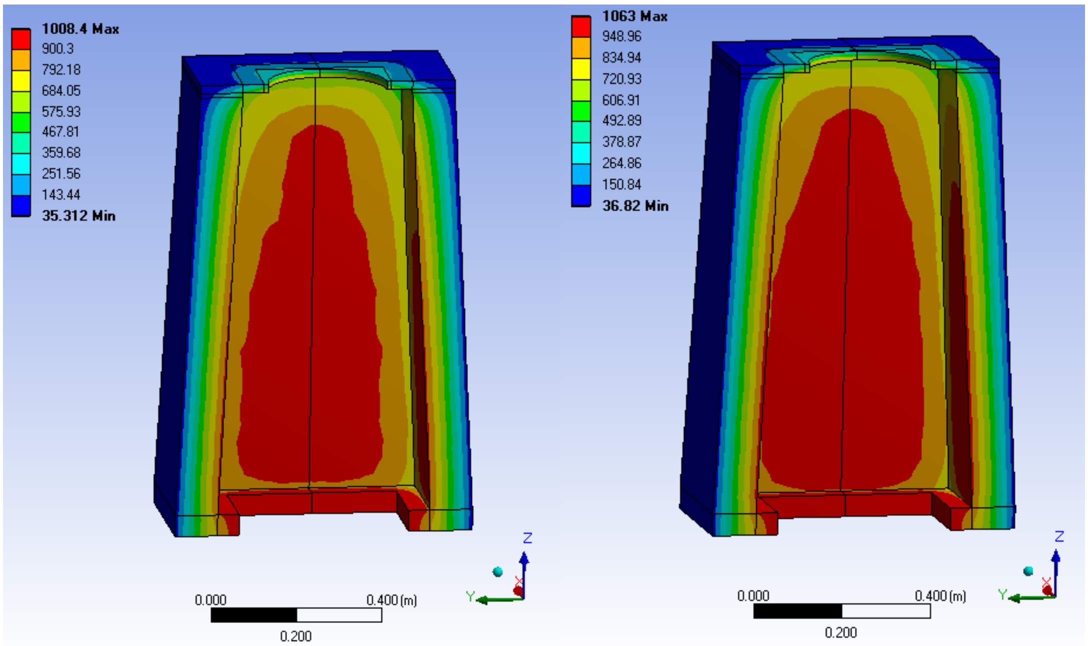

Figure 6.40. Temperature Field at Layer2. W/o and W/ Window.

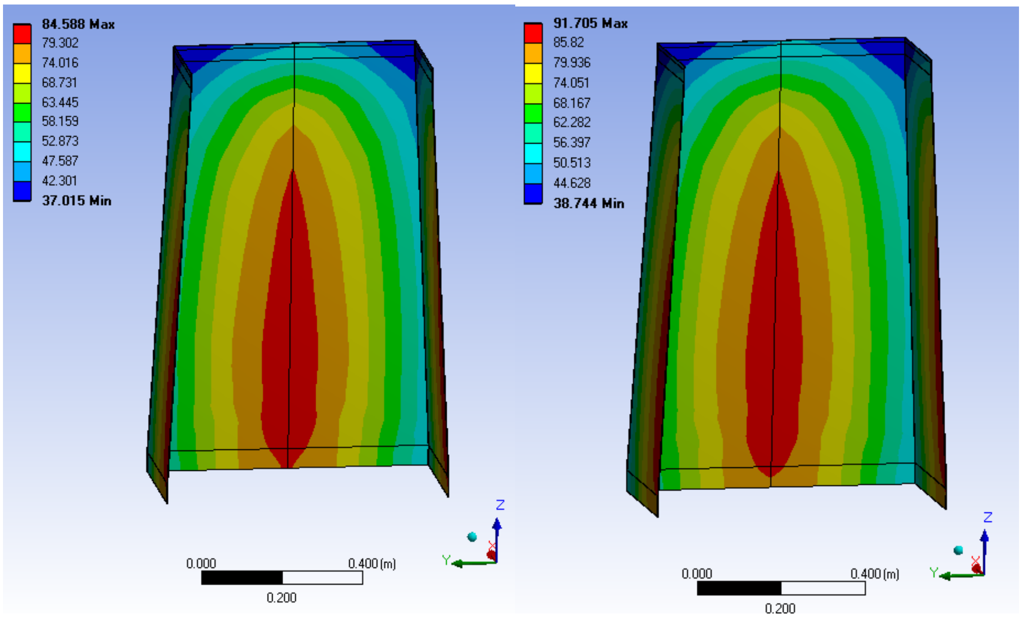

Figure 6.41. Temperature field at Layer 3. W/o and W/ Window.

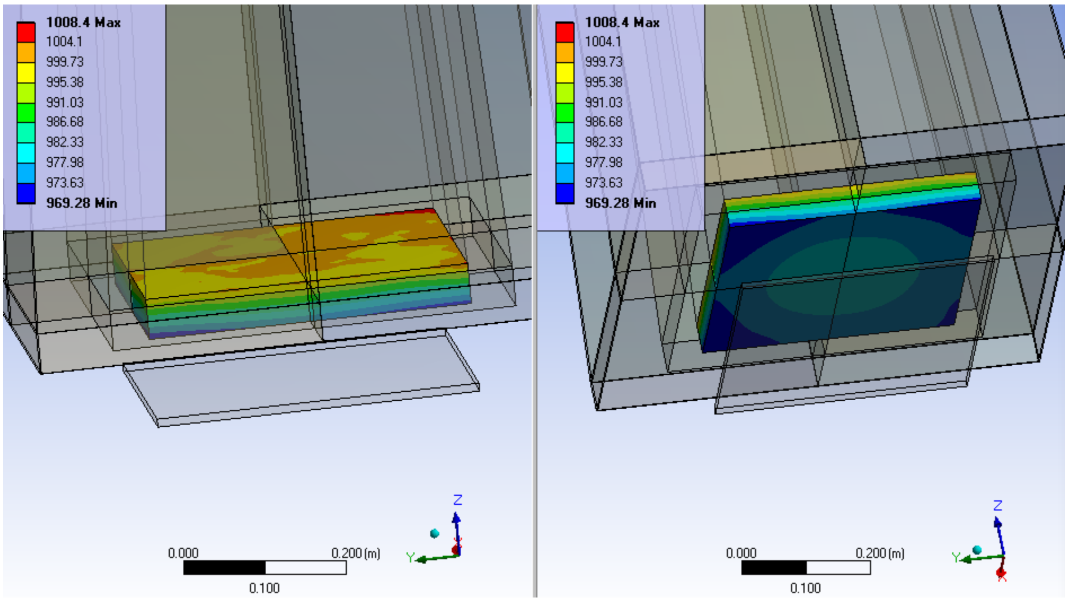

Figure 6.42. Temperature Field at the SiC plate. W/o Window.

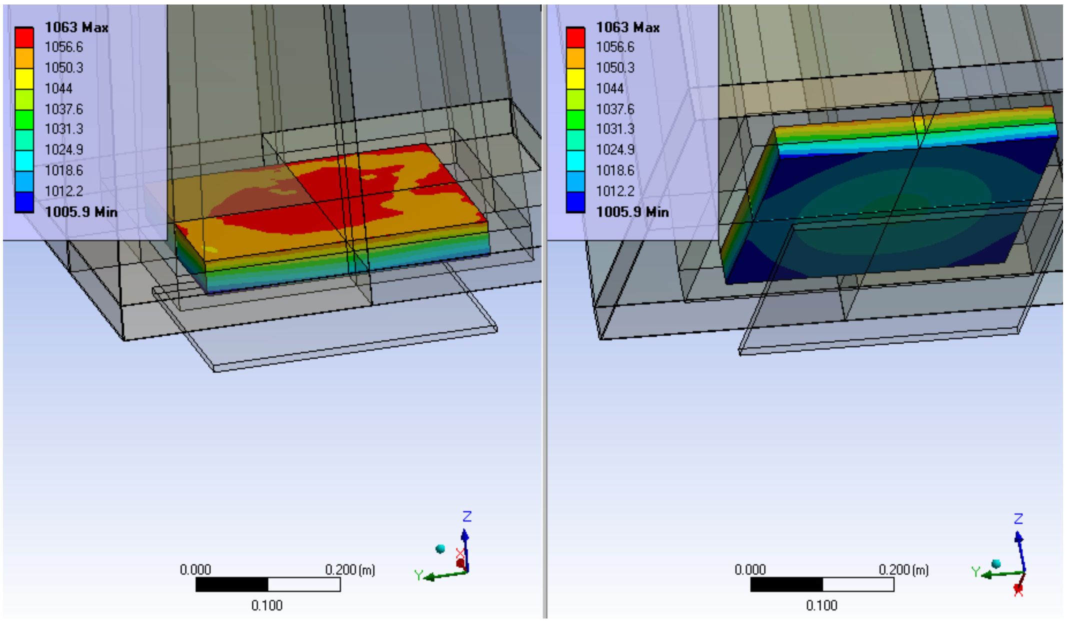

Figure 6.43. Temperature Field at the SiC plate. W/ Window.

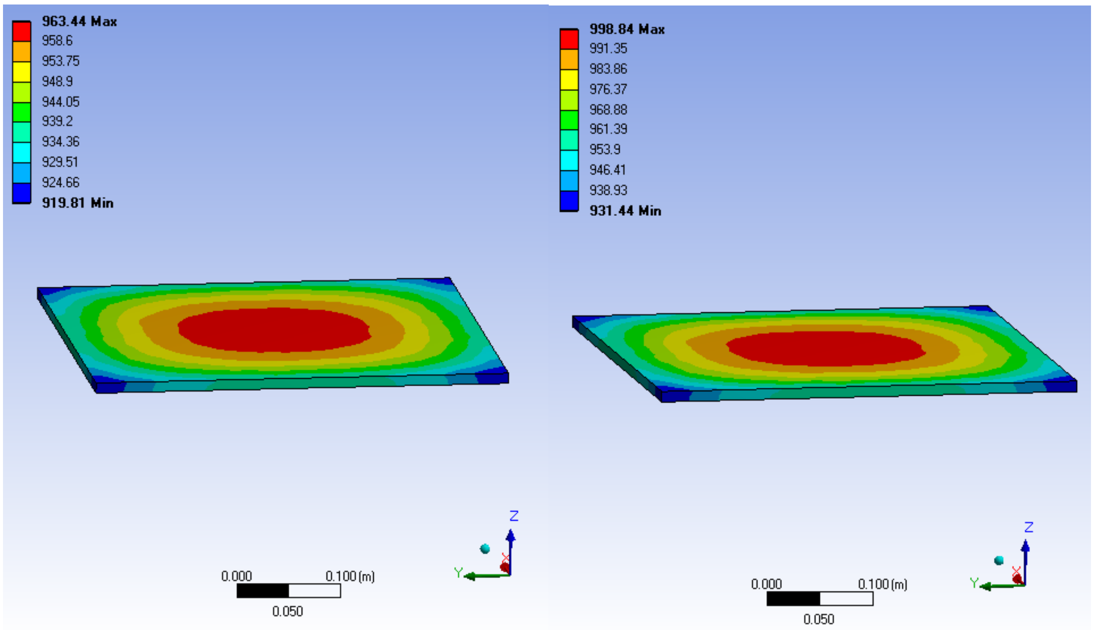

Figure 6.44. Temperature Field at the Limestone Layer. W/o and W/ Window.

Figures 6.42 and 6.43 shows the temperature field for the SiC plate, and 6.44 for the Limestone Layer. The temperature pattern presents symmetry with respect to an axis perpendicular to the plate and located at the centre.

Table 6.2.-Indirect Cavity SiC Solar Calciner Results Summary.

MODELO	PART	T_{MAX} [ºC]	$T_{allowed}$ [ºC]	Total Solar HF [W]	Total HF to Reactor [W]	Efficiency [%]
w/o window	Layer 1 Scuttherm	1179	1260	14607	2734	18.3
	Layer 2 Microtherm	1008	1150			
	Layer 3 AISI-304	85	870			
	SiC	1008	1500			
	Limestone	963	-			
W/ window	Layer 1 Scuttherm	1225	1260		4410	30
	Layer 2 Microtherm	1063	1150			
	Layer 3 AISI-304	92	870			
	SiC	1063	1500			
	Limestone	1000	-			

7. REFERENCES

7.1.1. Books

[1] Touloukian, Yeram Sarkis, and David P. DeWitt. Thermophysical properties of matter-the tprc data series. volume 7. thermal radiative properties-metallic elements and alloys. THERMOPHYSICAL AND ELECTRONIC PROPERTIES INFORMATION ANALYSIS CENTER LAFAYETTE IN, New York – Washington, 1970.

7.1.2. WWW resources

[1] SolTrace | Concentrating Solar Power | NREL [Online]. Available: https://www.nrel.gov/csp/soltrace.html [Accessed: 20-Dic-2018].

CONCLUSION

This document should serve as a guide for understanding the process followed to achieve the current engineering status of the integration of the solar power with the calciner reactor.

8. APPENDICES

8.1. Appendix A: Thermal Cooling Technologies S.L. mirror properties

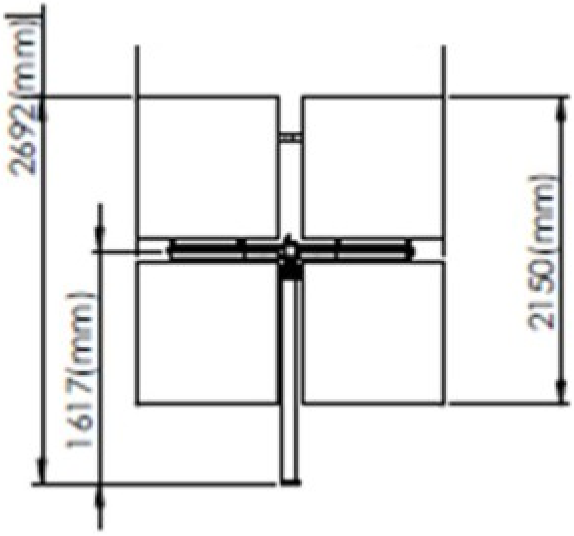

Optical efficiency: 93%

8.2. Appendix B: heliostat mirror properties

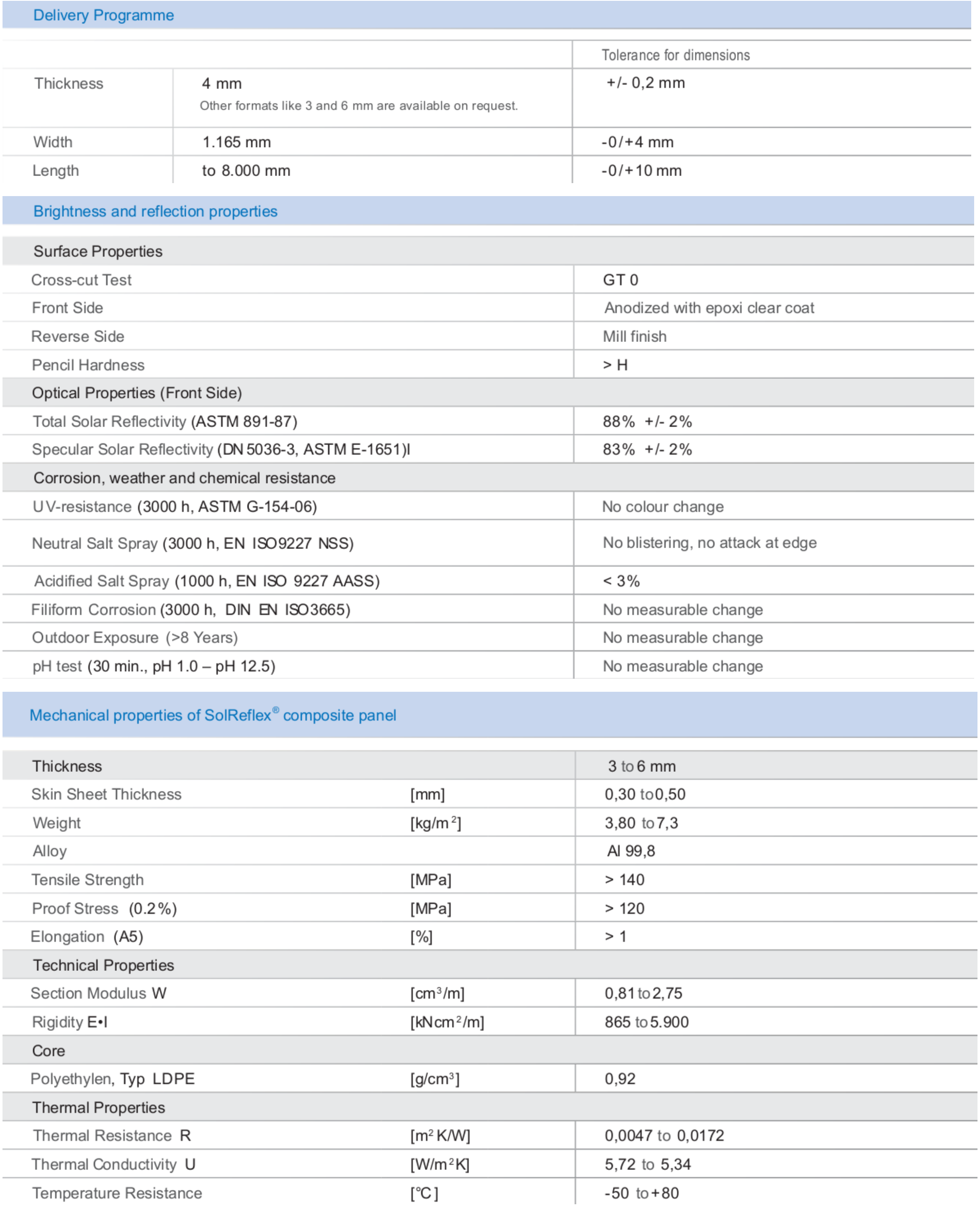

Delivery Programme

		Tolerance for dimensions
Thickness	4 mm Other formats like 3 and 6 mm are available on request.	+/- 0,2 mm
Width	1.165 mm	-0/+4 mm
Length	to 8.000 mm	-0/+10 mm

Brightness and reflection properties

Surface Properties	
Cross-cut Test	GT 0
Front Side	Anodized with epoxi clear coat
Reverse Side	Mill finish
Pencil Hardness	> H
Optical Properties (Front Side)	
Total Solar Reflectivity (ASTM 891-87)	88% +/- 2%
Specular Solar Reflectivity (DN 5036-3, ASTM E-1651)I	83% +/- 2%
Corrosion, weather and chemical resistance	
UV-resistance (3000 h, ASTM G-154-06)	No colour change
Neutral Salt Spray (3000 h, EN ISO9227 NSS)	No blistering, no attack at edge
Acidified Salt Spray (1000 h, EN ISO 9227 AASS)	< 3%
Filiform Corrosion (3000 h, DIN EN ISO3665)	No measurable change
Outdoor Exposure (>8 Years)	No measurable change
pH test (30 min., pH 1.0 – pH 12.5)	No measurable change

Mechanical properties of SolReflex® composite panel

Thickness		3 to 6 mm
Skin Sheet Thickness	[mm]	0,30 to 0,50
Weight	[kg/m^2]	3,80 to 7,3
Alloy		Al 99,8
Tensile Strength	[MPa]	> 140
Proof Stress (0.2%)	[MPa]	> 120
Elongation (A5)	[%]	> 1
Technical Properties		
Section Modulus W	[cm^3/m]	0,81 to 2,75
Rigidity E•I	[kNcm^2/m]	865 to 5.900
Core		
Polyethylen, Typ LDPE	[g/cm^3]	0,92
Thermal Properties		
Thermal Resistance R	[m^2 K/W]	0,0047 to 0,0172
Thermal Conductivity U	[W/m^{2}K]	5,72 to 5,34
Temperature Resistance	[°C]	-50 to +80

8.3. Appendix C: ICSiC-SC solar receiver material properties

Reflective walls:

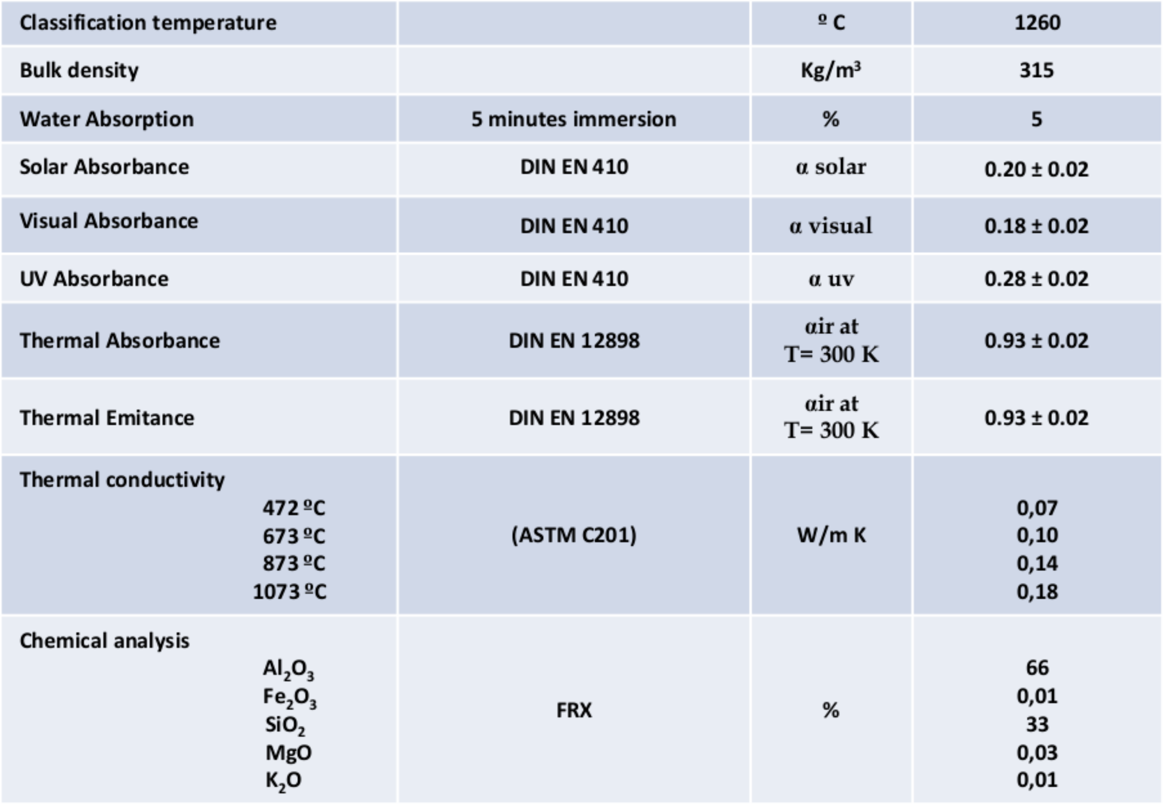

Classification temperature		**º C**	**1260**
Bulk density		**Kg/m³**	**315**
Water Absorption	**5 minutes immersion**	**%**	**5**
Solar Absorbance	**DIN EN 410**	**α solar**	**0.20 ± 0.02**
Visual Absorbance	**DIN EN 410**	**α visual**	**0.18 ± 0.02**
UV Absorbance	**DIN EN 410**	**α uv**	**0.28 ± 0.02**
Thermal Absorbance	**DIN EN 12898**	**αir at T= 300 K**	**0.93 ± 0.02**
Thermal Emitance	**DIN EN 12898**	**αir at T= 300 K**	**0.93 ± 0.02**
Thermal conductivity	**(ASTM C201)**	**W/m K**	
472 ºC			**0,07**
673 ºC			**0,10**
873 ºC			**0,14**
1073 ºC			**0,18**
Chemical analysis	**FRX**	**%**	
Al_2O_3			**66**
Fe_2O_3			**0,01**
SiO_2			**33**
MgO			**0,03**
K_2O			**0,01**

Thermal insulation:

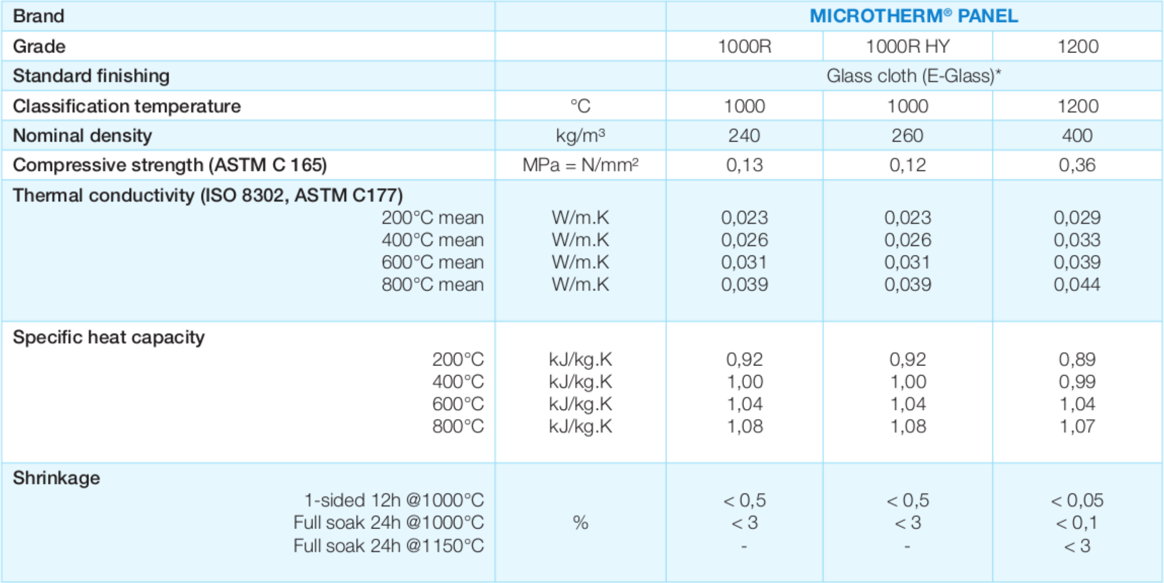

Brand		**MICROTHERM® PANEL**		
Grade		1000R	1000R HY	1200
Standard finishing		Glass cloth (E-Glass)*		
Classification temperature	°C	1000	1000	1200
Nominal density	kg/m³	240	260	400
Compressive strength (ASTM C 165)	MPa = N/mm²	0,13	0,12	0,36
Thermal conductivity (ISO 8302, ASTM C177)				
200°C mean	W/m.K	0,023	0,023	0,029
400°C mean	W/m.K	0,026	0,026	0,033
600°C mean	W/m.K	0,031	0,031	0,039
800°C mean	W/m.K	0,039	0,039	0,044
Specific heat capacity				
200°C	kJ/kg.K	0,92	0,92	0,89
400°C	kJ/kg.K	1,00	1,00	0,99
600°C	kJ/kg.K	1,04	1,04	1,04
800°C	kJ/kg.K	1,08	1,08	1,07
Shrinkage				
1-sided 12h @1000°C	%	< 0,5	< 0,5	< 0,05
Full soak 24h @1000°C		< 3	< 3	< 0,1
Full soak 24h @1150°C		-	-	< 3

Bottom Silicon Carbide plate:

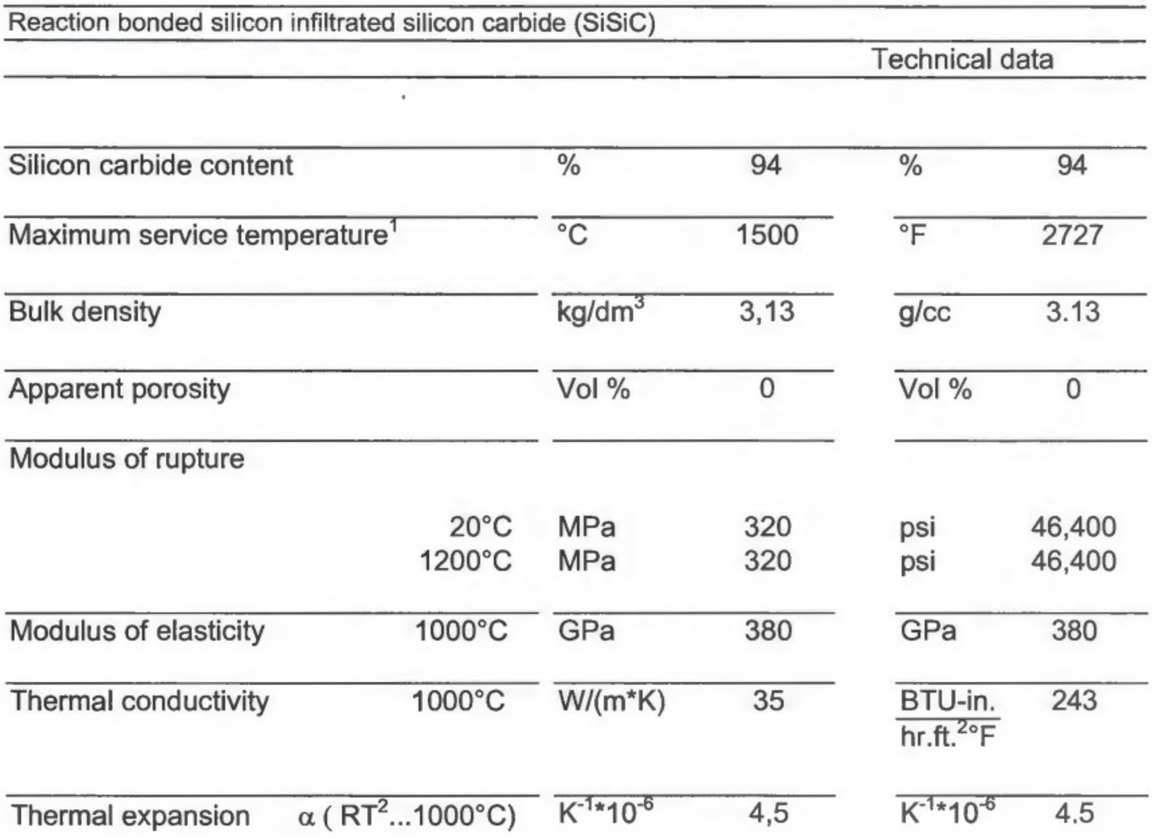

Reaction bonded silicon infiltrated silicon carbide (SiSiC)

		Technical data			
Silicon carbide content		%	94	%	94
Maximum service temperature[1]		°C	1500	°F	2727
Bulk density		kg/dm^3	3,13	g/cc	3.13
Apparent porosity		Vol %	0	Vol %	0
Modulus of rupture					
	20°C	MPa	320	psi	46,400
	1200°C	MPa	320	psi	46,400
Modulus of elasticity	1000°C	GPa	380	GPa	380
Thermal conductivity	1000°C	W/(m*K)	35	$\frac{\text{BTU-in.}}{\text{hr.ft.}^2{}^\circ\text{F}}$	243
Thermal expansion	α (RT[2]...1000°C)	$K^{-1}*10^{-6}$	4,5	$K^{-1}*10^{-6}$	4.5

8.4.Appendix D: Thermal radiative and solar optical properties of ICFC cavity.

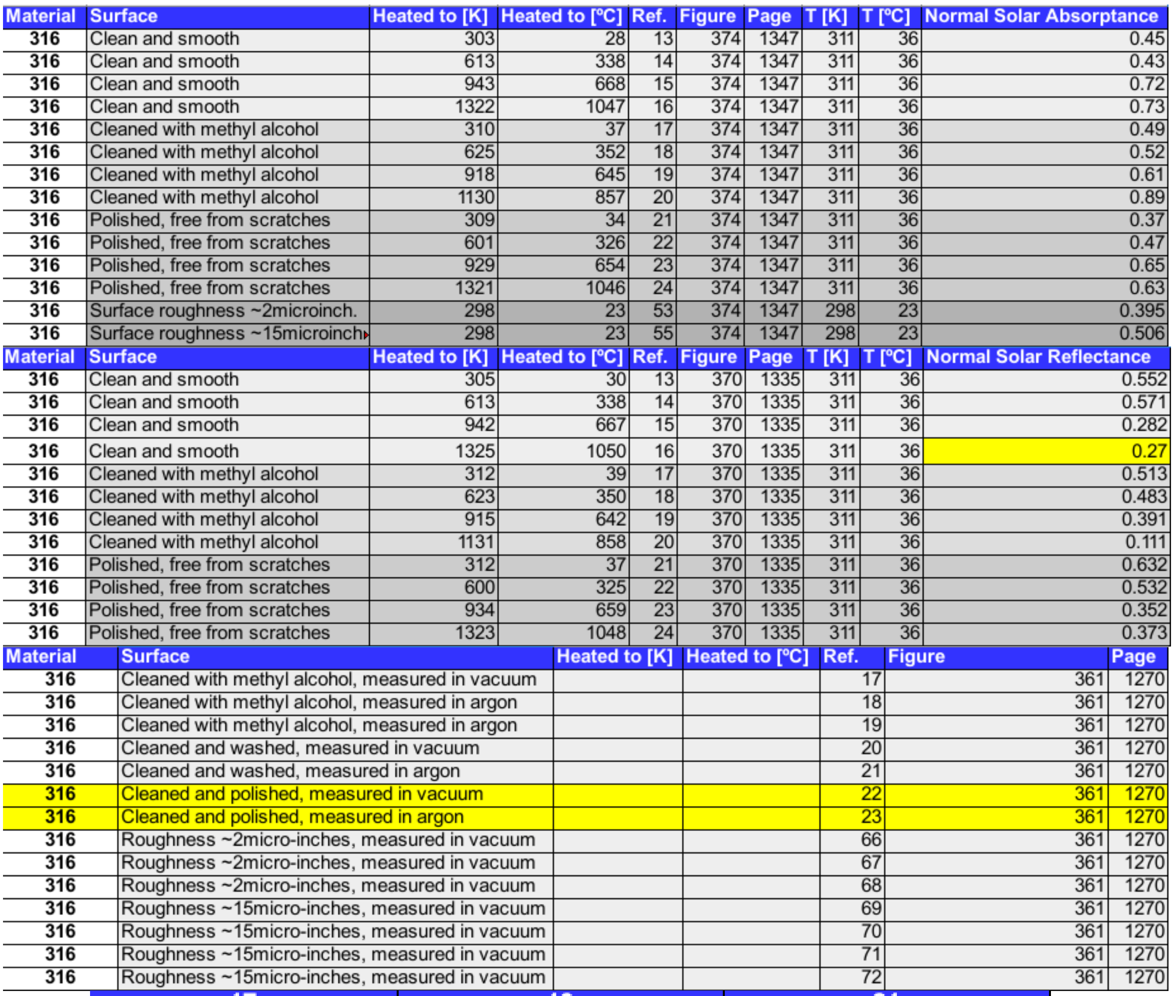

Material	Surface	Heated to [K]	Heated to [ºC]	Ref.	Figure	Page	T [K]	T [ºC]	Normal Solar Absorptance
316	Clean and smooth	303	28	13	374	1347	311	36	0.45
316	Clean and smooth	613	338	14	374	1347	311	36	0.43
316	Clean and smooth	943	668	15	374	1347	311	36	0.72
316	Clean and smooth	1322	1047	16	374	1347	311	36	0.73
316	Cleaned with methyl alcohol	310	37	17	374	1347	311	36	0.49
316	Cleaned with methyl alcohol	625	352	18	374	1347	311	36	0.52
316	Cleaned with methyl alcohol	918	645	19	374	1347	311	36	0.61
316	Cleaned with methyl alcohol	1130	857	20	374	1347	311	36	0.89
316	Polished, free from scratches	309	34	21	374	1347	311	36	0.37
316	Polished, free from scratches	601	326	22	374	1347	311	36	0.47
316	Polished, free from scratches	929	654	23	374	1347	311	36	0.65
316	Polished, free from scratches	1321	1046	24	374	1347	311	36	0.63
316	Surface roughness ~2microinch.	298	23	53	374	1347	298	23	0.395
316	Surface roughness ~15microinch	298	23	55	374	1347	298	23	0.506

Material	Surface	Heated to [K]	Heated to [ºC]	Ref.	Figure	Page	T [K]	T [ºC]	Normal Solar Reflectance
316	Clean and smooth	305	30	13	370	1335	311	36	0.552
316	Clean and smooth	613	338	14	370	1335	311	36	0.571
316	Clean and smooth	942	667	15	370	1335	311	36	0.282
316	Clean and smooth	1325	1050	16	370	1335	311	36	0.27
316	Cleaned with methyl alcohol	312	39	17	370	1335	311	36	0.513
316	Cleaned with methyl alcohol	623	350	18	370	1335	311	36	0.483
316	Cleaned with methyl alcohol	915	642	19	370	1335	311	36	0.391
316	Cleaned with methyl alcohol	1131	858	20	370	1335	311	36	0.111
316	Polished, free from scratches	312	37	21	370	1335	311	36	0.632
316	Polished, free from scratches	600	325	22	370	1335	311	36	0.532
316	Polished, free from scratches	934	659	23	370	1335	311	36	0.352
316	Polished, free from scratches	1323	1048	24	370	1335	311	36	0.373

Material	Surface	Heated to [K]	Heated to [ºC]	Ref.	Figure	Page
316	Cleaned with methyl alcohol, measured in vacuum			17	361	1270
316	Cleaned with methyl alcohol, measured in argon			18	361	1270
316	Cleaned with methyl alcohol, measured in argon			19	361	1270
316	Cleaned and washed, measured in vacuum			20	361	1270
316	Cleaned and washed, measured in argon			21	361	1270
316	Cleaned and polished, measured in vacuum			22	361	1270
316	Cleaned and polished, measured in argon			23	361	1270
316	Roughness ~2micro-inches, measured in vacuum			66	361	1270
316	Roughness ~2micro-inches, measured in vacuum			67	361	1270
316	Roughness ~2micro-inches, measured in vacuum			68	361	1270
316	Roughness ~15micro-inches, measured in vacuum			69	361	1270
316	Roughness ~15micro-inches, measured in vacuum			70	361	1270
316	Roughness ~15micro-inches, measured in vacuum			71	361	1270
316	Roughness ~15micro-inches, measured in vacuum			72	361	1270

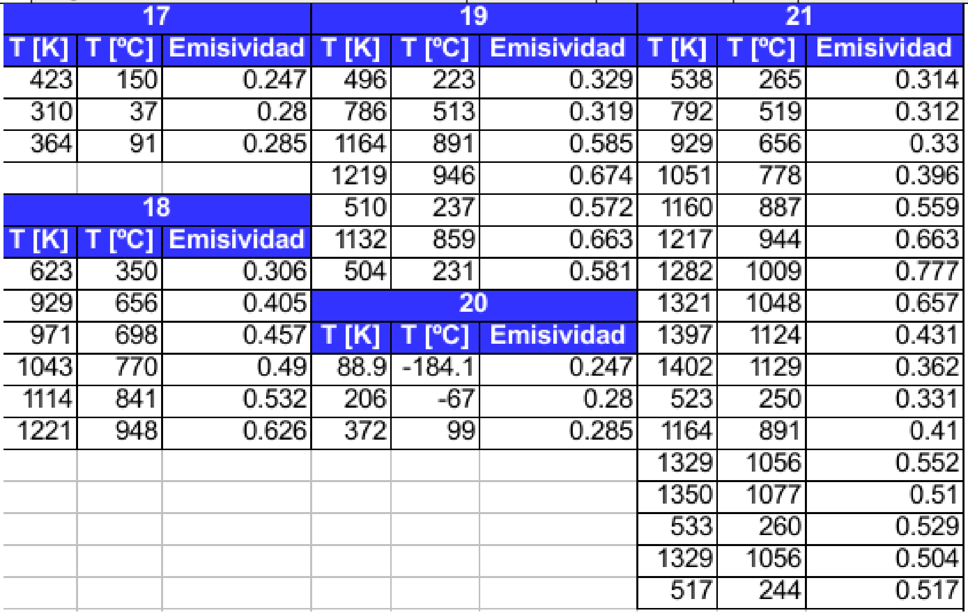

17		
T [K]	T [ºC]	Emisividad
423	150	0.247
310	37	0.28
364	91	0.285

18		
T [K]	T [ºC]	Emisividad
623	350	0.306
929	656	0.405
971	698	0.457
1043	770	0.49
1114	841	0.532
1221	948	0.626

19		
T [K]	T [ºC]	Emisividad
496	223	0.329
786	513	0.319
1164	891	0.585
1219	946	0.674
510	237	0.572
1132	859	0.663
504	231	0.581

20		
T [K]	T [ºC]	Emisividad
88.9	-184.1	0.247
206	-67	0.28
372	99	0.285

21		
T [K]	T [ºC]	Emisividad
538	265	0.314
792	519	0.312
929	656	0.33
1051	778	0.396
1160	887	0.559
1217	944	0.663
1282	1009	0.777
1321	1048	0.657
1397	1124	0.431
1402	1129	0.362
523	250	0.331
1164	891	0.41
1329	1056	0.552
1350	1077	0.51
533	260	0.529
1329	1056	0.504
517	244	0.517

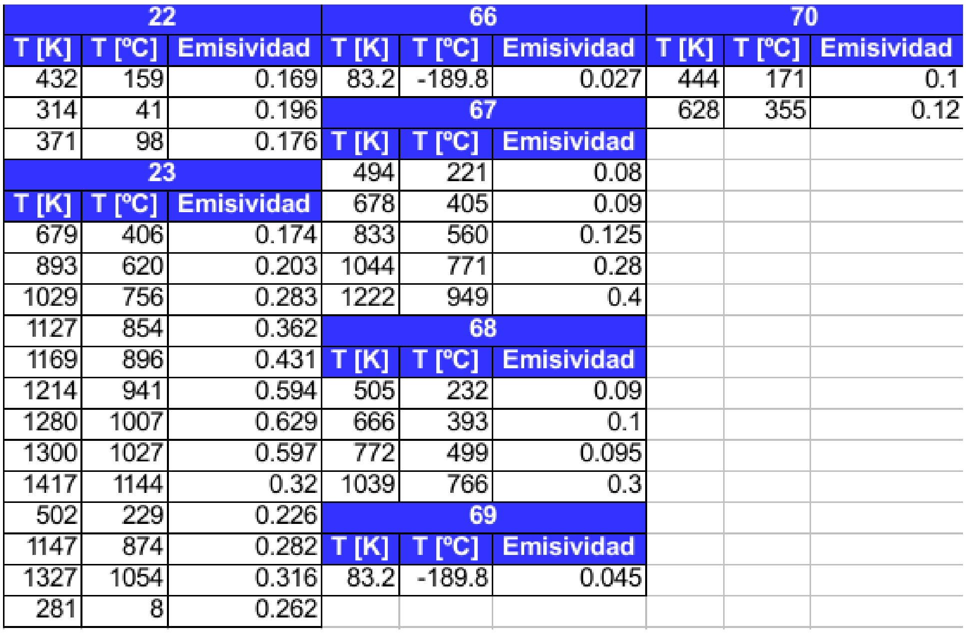

22		
T [K]	T [ºC]	Emisividad
432	159	0.169
314	41	0.196
371	98	0.176

23		
T [K]	T [ºC]	Emisividad
679	406	0.174
893	620	0.203
1029	756	0.283
1127	854	0.362
1169	896	0.431
1214	941	0.594
1280	1007	0.629
1300	1027	0.597
1417	1144	0.32
502	229	0.226
1147	874	0.282
1327	1054	0.316
281	8	0.262

66		
T [K]	T [ºC]	Emisividad
83.2	-189.8	0.027

67		
T [K]	T [ºC]	Emisividad
494	221	0.08
678	405	0.09
833	560	0.125
1044	771	0.28
1222	949	0.4

68		
T [K]	T [ºC]	Emisividad
505	232	0.09
666	393	0.1
772	499	0.095
1039	766	0.3

69		
T [K]	T [ºC]	Emisividad
83.2	-189.8	0.045

70		
T [K]	T [ºC]	Emisividad
444	171	0.1
628	355	0.12